JGR Atmospheres

RESEARCH ARTICLE
10.1029/2024JD042106

Key Points:

- Interactions between low-level jet and internal gravity waves were observed by Full Boundary Layer Turbulence Observation network
- Mechanisms are clarified behind turbulence intermittency involving internal and external factors
- Transitions and structural evolution are explained between strongly and weakly stable boundary layers

Supporting Information:

Supporting Information may be found in the online version of this article.

Correspondence to:

Y. Ren,
ry@lzu.edu.cn

Citation:

Ding, J., Ren, Y., Zhang, H., Chang, H., Hu, Z., Liang, J., et al. (2025). Mechanism of turbulence structure evolution in the nocturnal boundary layer during the interaction of low-level jet and internal gravity waves: Based on full boundary layer turbulence observations. *Journal of Geophysical Research: Atmospheres*, *130*, e2024JD042106. https://doi.org/10.1029/2024JD042106

Received 31 JUL 2024
Accepted 14 MAR 2025

Author Contributions:

Conceptualization: Jie Ding, Hongsheng Zhang
Data curation: Zeyong Hu, Shujin Wang
Formal analysis: Jie Ding, Yan Ren, Heying Chang, Jiening Liang, Xianjie Cao, Pengfei Tian, Lei Zhang
Methodology: Jie Ding, Yan Ren, Hongsheng Zhang
Resources: Kaijun Zhang
Supervision: Zeyong Hu, Lei Zhang
Visualization: Jie Ding, Heying Chang
Writing – original draft: Jie Ding, Yan Ren

Mechanism of Turbulence Structure Evolution in the Nocturnal Boundary Layer During the Interaction of Low-Level Jet and Internal Gravity Waves: Based on Full Boundary Layer Turbulence Observations

Jie Ding[1,2,3,4], Yan Ren[1], Hongsheng Zhang[5], Heying Chang[1], Zeyong Hu[2], Jiening Liang[6], Kaijun Zhang[3], Shujin Wang[2], Xianjie Cao[6], Pengfei Tian[6], and Lei Zhang[1,6]

[1]Collaborative Innovation Center for Western Ecological Safety, Lanzhou University, Lanzhou, China, [2]Key Laboratory of Cryospheric Science and Frozen Soil Engineering, Northwest Institute of Eco-Environment and Resources, Chinese Academy of Sciences, Lanzhou, China, [3]Gansu Sub-Bureau of Northwest Air Traffic Management Bureau of Civil Aviation of China, Lanzhou, China, [4]University of Chinese Academy of Sciences, Beijing, China, [5]Laboratory for Climate and Ocean-Atmosphere Studies, Department of Atmospheric and Oceanic Sciences, School of Physics, Peking University, Beijing, China, [6]Key Laboratory for Semi-Arid Climate Change of the Ministry of Education, College of Atmospheric Sciences, Lanzhou University, Lanzhou, China

Abstract In a stable boundary layer (SBL), turbulence is generally weak and exhibits significant intermittent characteristics. Interactions among motions of different scales complicate its structural evolution, making prediction challenging. This study focuses on two typical processes in the SBL: low-level jet (LLJ) and internal gravity waves (IGWs), investigating how their interactions influence the evolution of turbulence structures. Utilizing a full boundary layer turbulence observation network and data processing system at Zhongchuan International Airport, this study includes eddy covariance system, Doppler Lidar, and wind profiling radar. In strongly SBL, turbulence energy accumulates in higher layers and, during downward transfer, generates local LLJ and IGWs, triggering intermittent turbulence events. Internal factors of turbulence intermittency dominated the process. The interaction between LLJ and IGWs maintains intermittent turbulence bursts, accompanied by the conversion of sub-mesoscale energy to turbulent energy. In weakly SBL, the conversion of sub-mesoscale motion energy drives intermittent turbulence events, along with energy transfers between different scales of IGWs, resulting in weaker turbulence intermittency. External factors of turbulence intermittency dominated the process. In both cases, the interaction between LLJ and IGWs alters turbulence structure and atmospheric stability. Turbulent mixing changes the mean gradient field, further influencing the LLJ height. This study elucidates the mechanisms of interaction between internal and external factors in turbulence intermittency. It outlines energy transfer among different scales of motion and clarifies the mechanisms behind state transitions and structural evolution in strongly and weakly SBL. These findings are significant for advancing theoretical research and simulation developments of the SBL.

Plain Language Summary The study focuses on the complex behavior of turbulence in the stable boundary layer (SBL), which often features weak and intermittent turbulence, posing challenges for prediction with current models. Turbulence intermittency is an inherent feature of the SBL and can be driven by internal factors (wind shear and stratification) and external factors (sub-mesoscale disturbances). Sub-mesoscale motions are common and always mixed together in the SBL, such as internal gravity waves (IGWs) with different periods. Using a turbulence observational network, this study investigates how the interaction of low-level jets (LLJ) with IGWs induces intermittent turbulence and affects the turbulence structure of the SBL. In the strongly SBL, the internal factor triggers the turbulent intermittency, and the sub-mesoscale disturbances sustain turbulence bursts, transfer energy to smaller-scale motions, and alter the structure and state of the SBL. In the weakly SBL, the sub-mesoscale disturbances trigger the turbulent intermittency, transferring energy to larger or smaller-scale motions, resulting in weaker turbulent bursts. These findings are significant for improving the theoretical understanding and modeling of SBL dynamics, particularly in predicting turbulence intensity and transitions between different stability states.

1. Introduction

The atmospheric boundary layer is the lowest part of the atmosphere and is directly affected by human activity. Turbulence is the primary form of motion in the atmospheric boundary layer. Thus, turbulence directly affects the transport and exchange of materials and energy, thereby exerting a significant influence on practical issues such as air pollution (Ren et al., 2019, 2021), wind power generation (Wilczak et al., 2019), and aviation safety (Kim et al., 2018). Currently, there is a significant lack of understanding and research regarding the atmospheric boundary layer, particularly the stable boundary layer (SBL) (Lemone et al., 2018). Turbulent motion in the SBL is relatively weak, easily influenced by sub-mesoscale motions (the motions between the primary turbulent eddies and smallest mesoscale motions defined by Mahrt (2014)), and characterized by significant intermittency (Allouche et al., 2022), which may be related to decoupling from the surface. As a result, the vertical structure no longer follows traditional theories (Mahrt, 2014). The SBL flow field is often a complex mixture of motions of different scales (Mahrt, 2010), making understanding and simulating the SBL very challenging (Mahrt & Bou-Zeid, 2020; Schiavon et al., 2023). Therefore, studying the turbulence structure of the full boundary layer and its evolution mechanism during the interaction of motions at different scales in the SBL is important for advancing theoretical research and simulation development of the SBL.

Turbulent intermittency refers to the occurrence of short-lived, explosive, and more active turbulent motions within weak turbulence or laminar flow (Mahrt, 1998), which includes periods of quiescence and bursting. Burst turbulence can alter the state of the SBL, leading to abrupt changes in the SBL structure (Chang et al., 2024; Ren et al., 2023). Sun et al. (2012, 2016) used the relationship between turbulent intensity and wind speed to separate three regimes of SBL and three types of intermittency mechanisms which is known as HOckey-Stick Transition (HOST). In the SBL, many atmospheric processes can drive the burst of intermittent turbulence (Ren et al., 2023), such as wind shear generated by low-level jet (LLJ) and disturbances from sub-mesoscale motions (Mahrt, 2014). Sub-mesoscale motions triggering turbulence intermittency have been noted in field observations include, but are not limited to, drainage flows (Hiscox et al., 2023), horizontal meandering (Mortarini et al., 2019), internal gravity waves (IGWs) (Sun, Mahrt, et al., 2015), and small-scale fronts (Mahrt, 2019). Businger (1973) proposed that the interaction between wind shear and stable stratification in the strongly SBL during clear nights can lead to periodic bursts of intermittent turbulence, which is considered as an internal factor in the occurrence of turbulent intermittency (Allouche et al., 2022). Correspondingly, sub-mesoscale motions are regarded as external factors (Mahrt, 2014). In the actual atmosphere, the interaction between internal and external factors driving the burst of turbulent intermittency makes the physical origin of these bursts highly complex, hindering our understanding and prediction of the SBL structure evolution.

LLJs are significant processes in the nocturnal SBL, possibly caused by inertial oscillations (Shibuya et al., 2014), baroclinicity associated with sloping terrain (Holton, 1967), and large-scale meteorological forcing (Shapiro et al., 2016). The inertial oscillation mechanism of the LLJs is closely related to the internal factors of turbulent intermittency (Allouche et al., 2022; Businger, 1973; Van der Linden et al., 2020). The wind shear generated near LLJ transfers turbulent kinetic energy downward, significantly impacting surface turbulence characteristics, deepening the boundary layer, and enhancing turbulent mixing. This is a primary energy source for maintaining vertical mixing in the nocturnal SBL (Brunsell et al., 2021; Duarte et al., 2015; Tsiringakis et al., 2022). The presence of nocturnal LLJ complicates the turbulence structure of the boundary layer, leading to inaccuracies in boundary layer parameterization schemes. This is a significant factor contributing to systematic bias of near-surface temperature and wind speed (Banta et al., 2007; Barlow et al., 2015; Holtslag et al., 2013; Tsiringakis et al., 2022; Wei et al., 2023).

Sub-mesoscale motions, such as IGWs and Kelvin-Helmholtz instabilities, are non-stationary movements that are larger in scale than turbulence (Mahrt, 2014) and are commonly observed in the SBL. Locally generated IGWs have temporal and spatial scales in the sub-mesoscale range. IGWs are buoyancy oscillations formed under the influence of buoyancy and gravity that propagate through alternating convergence and divergence in the horizontal and vertical directions (Nappo, 2012; Sutherland et al., 2020; Wei et al., 2022). IGWs can be induced by physical processes such as heterogeneous terrain, strong wind shear near LLJ, buoyancy instability generated by convection, slope oscillations, and cold fronts (Chemel et al., 2009; Luo & Fritts, 1993; Mortarini et al., 2018; Román-Cascón et al., 2015; Sarkar & Scotti, 2017; Viana et al., 2010, 2012). Different scales of motion in the SBL are often mixed. However, previous studies have predominantly focused on independent analyses of different scales of motion, such as independent analyses of LLJ and IGWs (Brunsell et al., 2021; Cava et al., 2015;

Tsiringakis et al., 2022). Some studies have focused on the interactions between near-surface waves and turbulence (Barbano et al., 2022; Roy et al., 2021). To date, the physical mechanisms of interactions between different scales of motion (such as typical LLJ and IGWs) in the SBL and their impact on the turbulence structure of the boundary layer remain unclear.

The study of nocturnal full boundary layer structures is limited by observations. LLJs are identified by the maximum wind speed and wind shear in the wind profiles. Wind profile data can be obtained from sounding balloons, wind profiling radar (WPR), Sodar, and Lidar. However, the observation frequency of sounding balloons is limited, and the process of splicing and calibrating data with different spatial resolutions from the low-, medium-, and high-detection modes of WPR can lead to data fusion errors. Sodar can reveal the dynamic characteristics of the vertical structure of thermal turbulence in the atmospheric boundary layer, but it has limitations, including restricted measurement height, susceptibility to environmental noise, and complex signal processing (Kallistratova & Kouznetsov, 2012). Owing to its high-quality detection, high spatiotemporal resolution, and portability, Lidar has been widely used in the study of LLJ (Roy et al., 2021; Tsiringakis et al., 2022; Wildmann et al., 2019). However, observing the full boundary layer turbulence structure is difficult. The eddy covariance system is the most commonly used method for observing atmospheric turbulence, but its height limitation mainly restricts its use to the study of near-surface turbulence structures. It is unrealistic to establish an eddy covariance system for observing atmospheric turbulence throughout the full boundary layer. Therefore, some studies have developed algorithms to estimate the turbulence using remote sensing data (Borque et al., 2016; Smalikho & Banakh, 2017; Solanki et al., 2022). For example, Bodini et al. (2019) used Lidar to estimate the turbulent dissipation rate (TDR, ε) to study the spatial turbulence over a complex terrain. Therefore, obtaining a full boundary turbulence observation is important for studying the evolution of the spatial turbulence structure in the SBL.

The complex topography of the Loess Plateau frequently exhibits sub-mesoscale motions within the SBL (Chang et al., 2024), and LLJ occur frequently. The full boundary layer turbulence observation experiment was constructed at the Lanzhou Zhongchuan International Airport, located on the Loess Plateau, by combining near-surface eddy covariance instruments, WPR, Lidar, and conventional meteorological observations. A data processing system for estimating full boundary layer turbulence was developed by integrating multiple data sources, scanning techniques, and derivation algorithms. The observational network and data processing system will be introduced in Section 2. Based on the network and system, two typical cases of interactions between LLJ and IGWs were selected to analyze the evolution mechanism of the nocturnal SBL turbulence structure, which will be detailed in Section 3. Finally, Section 4 summarizes the main conclusions of the paper.

2. Data and Methods

2.1. Data

Observational data for this study were obtained from the Zhongchuan International Airport (ZCIA) Atmospheric Physics and Atmospheric Environment Continuous Observation Station (36°31′N, 103°36′E) in Lanzhou, China. The site is located in the northwest of Lanzhou, on the Loess Plateau, at an altitude of 1,947 m, as shown in Figure 1a. The terrain of the Loess Plateau is complex, predominantly mountainous, and represents a typical complex underlying surface (Chang et al., 2024).

At this site, we established a FBLTO network, consisting of a Doppler Lidar (Lidar, Windcube 400s-at, Leosphere, France), WPR (CLC-11-D), an automatic weather observing system (AWOS, Vaisala, Finland) at a height of 1.5 m, a two-dimensional ultrasonic anemometer (WMT702, Vaisala, Finland) at a height of 10 m, and an eddy covariance system (EC) at a height of 2.7 m, as shown in the schematic distribution in Figure 1b. The Lidar was operated in the vertical mode using Doppler Beam Swinging with a 75° elevation angle to obtain mid-to-upper-level wind profiles and in the tilted mode with a 3° elevation angle in the northward direction to obtain boundary layer spatial turbulence structures, with a temporal resolution of 5 min. Low-level wind profile data were provided by the WPR, with a sampling period of 6 min. The AWOS and two-dimensional ultrasonic anemometer provided conventional meteorological parameters such as temperature, pressure, humidity, and horizontal wind speed and direction. The eddy covariance system consisted of a three-dimensional sonic anemometer (CSAT-3, Campbell Scientific Co., USA) and an open-path infrared gas analyzer (LI7500A, LICOR Biosciences, USA). EC was used to obtain 10 Hz data on three-dimensional wind speed, temperature, water vapor density, and CO_2 concentration. The WMT702 was used to measure 15 s data on two-dimensional wind speed.

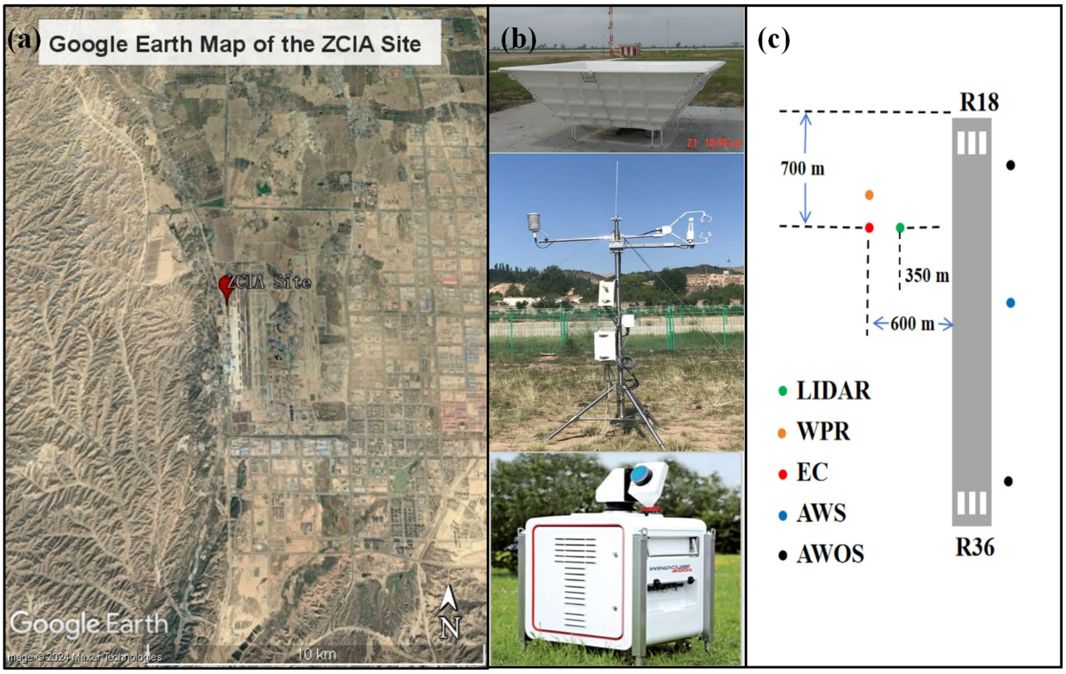

Figure 1. Topography and instrument layout at the ZCIA site: (a) Google Maps view of the observation site, with the red marker indicating the location of the observation station; (b) instruments: wind profiling radar (WPR), eddy covariance system (EC), and Doppler Lidar (Lidar); (c) Schematic diagram of the instrument distribution.

Given the characteristics of the detection instruments in terms of data quality, spatiotemporal resolution, and scanning modes, we developed a Full Boundary Layer Turbulence Data Processing System (FBLTDPS). The data processing system consists of three modules: data preprocessing, wind data fusion, and TDR estimation. In the data preprocessing module, both Lidar and WPR are processed, including gap filling, outlier removal, and median filtering for noise reduction. Turbulence data are further processed using Eddy Pro software (Advanced mode, Version 6.2.1, LI-COR Biosciences, Inc., USA), which includes outlier removal, secondary coordinate rotation, trend removal, and necessary corrections for turbulence fluxes, such as humidity corrections for sonic virtual temperature and Webb-Pearman-Leuning (WPL) corrections. A 30 min block averaging interval, applied within the Reynolds averaging framework, is used to detect spectral gaps and reconstruct the turbulence data (Ren et al., 2019). In the wind data fusion module, multi-source wind data from the FBLTO network are integrated to provide wind field information below 1,500 m. Specifically, wind field data from 400 to 1,500 m are provided by Lidar-DBS, while additional data sources, including WPR (100–400 m), ultrasonic anemometers (10 m), and three-dimensional sonic anemometers (2.7 m), supply information for the Lidar blind zone (below 400 m). The fused wind field data includes horizontal wind speed and direction, with a temporal resolution of 30 min. The TDR estimation module consists of two components: near-surface and spatial structure estimations. Near-surface TDR is estimated using the second-order structure function method, based on three-dimensional sonic anemometer data at 2.7 m. Spatial TDR (21–500 m) is estimated using the azimuthal structure function method, based on Lidar tilted-mode scans.

2.2. Methods

2.2.1. Turbulence Statistical Parameters

The specific definitions and calculation procedures for the turbulence statistical parameters used in this study are described below. The turbulent kinetic energy (TKE) is defined as follows:

$$\mathrm{TKE} = \frac{1}{2}\left(\overline{{u'_{\mathrm{turb}}}^2} + \overline{{v'_{\mathrm{turb}}}^2} + \overline{{w'_{\mathrm{turb}}}^2}\right), \tag{1}$$

Where u'_{turb}, v'_{turb}, and w'_{turb} are the three-dimensional velocity fluctuations of the turbulence.

The flux Richardson number (R_{if}) is used to represent atmospheric stability:

$$R_{if} = \frac{g}{\overline{\theta_v}}\overline{w'\theta_v'} \Big/ \overline{u'w'}\frac{\partial \overline{u}}{\partial z}, \tag{2}$$

where g is the gravitational acceleration, $\overline{\theta_v}$ is the virtual potential temperature, and z denotes the height.

2.2.2. Quantitative Characterization of Sub-Mesoscale Motion and Turbulent Intermittency

The automatic algorithm for the separation and reconstruction of sub-mesoscale motions and turbulence (SMT), which was proposed and improved by Ren et al. (2019, 2023) is used to detect and quantitatively characterize the turbulent intermittency events at the near-surface. The algorithm checks the Hilbert spectrum of observational data to identify spectral gaps between large-scale and small-scale motions, using these gaps to reconstruct the turbulent motion sequence and separate sub-mesoscale motions from collected signals. During this process, the statistics of sub-mesoscale motions near-surface are also characterized quantitatively. We applied SMT to high-frequency three-dimensional wind speed and temperature data from near-surface observations. The effectiveness of the SMT has been validated in various studies across different underlying surfaces (Chang et al., 2024). The SMT method involves three main steps: First, the 10 Hz turbulent fluctuation data within a 30 min interval are decomposed into intrinsic mode functions (IMFs) using empirical mode decomposition. Next, the second-order Hilbert marginal spectrum of turbulence deviations is calculated to identify spectral gaps between small- and large-scale motions. Finally, the turbulent and sub-mesoscale motion components are reconstructed by combining IMFs with frequencies above and below the gap frequencies, respectively. The parameters for quantitatively characterizing turbulent intermittency include the local intermittent strength of turbulence (LIST) and intermittency strength (IS), which reflect the kinetic and potential energy intermittency features:

$$\text{LIST} = \text{C}_{\text{KE}}\text{LIST}_{\text{KE}} + \text{C}_{\text{PE}}\text{LIST}_{\text{PE}}, \tag{3}$$

$$\text{IS} = \text{C}_{\text{KE}}\text{IS}_{\text{KE}} + \text{C}_{\text{PE}}\text{IS}_{\text{PE}}, \tag{4}$$

where LIST represents the proportion of turbulence energy in the total energy, and LIST_{KE} and LIST_{PE} represent the intermittent strength indices of the kinetic and potential energy, respectively. $\text{LIST}_{\text{KE}} = \sqrt{\text{TKE}}/\sqrt{\text{TKE} + \text{SKE}}$, where TKE is the turbulent kinetic energy $\text{TKE} = \frac{1}{2}\left(\overline{u'^2_{\text{turb}}} + \overline{v'^2_{\text{turb}}} + \overline{w'^2_{\text{turb}}}\right)$, and SKE is the kinetic energy of sub-mesoscale motion $\text{SKE} = \frac{1}{2}\left(\overline{u'^2_{\text{sub}}} + \overline{v'^2_{\text{sub}}} + \overline{w'^2_{\text{sub}}}\right)$. $\text{LIST}_{\text{PE}} = \sqrt{|\text{TPE}|}/\sqrt{|\text{TPE}| + |\text{SPE}|}$. Zilitinkevich et al. (2007) introduced the concept of turbulent potential energy (TPE) and defined the turbulent total energy (TTE) as the sum of TKE and TPE (TTE = TKE + TPE). $\text{TPE} = \frac{1}{2}(g/T_0N_{bv})^2\overline{\theta'^2_{\text{turb}}}$, and SPE is the potential energy of sub-mesoscale motion, $\text{SPE} = \frac{1}{2}(g/T_0N_{bv})^2\overline{\theta'^2_{\text{sub}}}$, where N_{bv} denotes the Brunt–Väisälä frequency, as in Equation 6. IS is the ratio of the sub-mesoscale energy to the turbulence energy. Both indicators are designed to capture the intensity of intermittent turbulence, with IS specifically highlighting the contribution of sub-mesoscale motion. $\text{IS}_{\text{KE}} = \sqrt{\text{SKE}}/\sqrt{\text{TKE}}$, and $\text{IS}_{\text{PE}} = \sqrt{|\text{SPE}|}/\sqrt{|\text{TPE}|}$. C_{KE} and C_{PE} represent the contributions of LIST_{KE} (IS_{KE}) and LIST_{PE} (IS_{PE}) to LIST (IS), respectively, which are expressed as follows: $C_{\text{KE}} = \frac{\text{TKE}}{\text{TKE}+|\text{TPE}|}$, $C_{\text{PE}} = \frac{|\text{TPE}|}{\text{TKE}+|\text{TPE}|}$, and $C_{\text{KE}} + C_{\text{PE}} = 1$. According to the above definition, a LIST value closer to 1 (IS closer to 0) indicates that turbulent motion occupies a larger proportion of the original signal, with less influence from sub-mesoscale motion, resulting in weaker intermittency of the turbulence, and vice versa.

2.2.3. Quadrant Analysis

Quadrant analysis decomposes the instantaneous flux of any pair of turbulent variables into four contributions from coherent turbulent structures, thereby quantitatively identifying and characterizing large-scale coherent structures in the atmospheric boundary layer (Guo et al., 2022; Wallace, 2016; Wallace et al., 1972), primarily focusing on the analysis of turbulent observations. Based on their primary features, these coherent structures are defined as follows (Francone et al., 2012): Q1 is the outward interaction, Q2 is the ejection, Q3 is the inwards interaction, and Q4 is the sweep, representing the modes of turbulence diffusion outward, upward, inward, and downward, respectively. To reflect the relative importance of upward ejection and downward sweep motions in the momentum flux, the flux contribution difference between downward sweep and upward ejection motions is defined as $\Delta S_{SW\text{-}EJ}$ (Guo et al., 2022):

$$\Delta S_{SW-EJ} = \frac{\overline{u'w'}_{IV}}{\overline{u'w'}} - \frac{\overline{u'w'}_{II}}{\overline{u'w'}}, if \overline{u'w'} < 0, \tag{5}$$

where *II* and *IV* represent the second (Q2) and fourth (Q4) quadrants, respectively. While $\Delta S_{SW\text{-}EJ} > 0$ indicates that the near-surface turbulent motion is dominated by sweeps, while $\Delta S_{SW\text{-}EJ} < 0$ indicates that the near-surface turbulent motion is dominated by ejections.

2.2.4. Identification of LLJ and IGWs

Following previous studies, this study identifies LLJs over the ZCIA site from January 2021 to December 2022 by examining the vertical profiles of horizontal wind speed and vertical wind shear (Banta et al., 2006, 2007; Bonner, 1968). LLJs over the ZCIA site predominantly occur during the nocturnal period (64.1%), with a low jet axis height (53.6% of LLJ below 500 m), as detailed in Table S1 in Supporting Information S1. Therefore, it is important to study the effect of the LLJs over this site on the turbulence structures of the nocturnal boundary layer. As suggested by Banta (2008), the definition of LLJ depends on the specific application and is also constrained by the data set used. To more accurately capture the characteristics of LLJs in the SBL, we also refer to the LLJ criteria outlined by Whiteman et al. (1997) and Miao et al. (2018).

In atmospheric boundary layer research, three features are commonly detected to identify IGWs: (a) wave-like characteristics (Cava et al., 2019; Roy et al., 2021; Sun, Mahrt, et al., 2015; Wei et al., 2022), (b) period (frequency) analysis through wavelet analysis (Corrêa et al., 2021; Sun, Mahrt, et al., 2015; Wei et al., 2022), and (c) antiphase relationships (Sun, Mahrt, et al., 2015). In stable stratification, the propagation of buoyancy oscillations leads to the formation of IGWs. Hence, buoyancy oscillations, which are prerequisites for generating IGWs, can be used for their identification. The frequency of buoyancy oscillations is referred to as the Brunt–Väisälä frequency, which is defined as follows:

$$N_{bv} = \sqrt{\frac{g}{\overline{\theta}} \frac{\partial \overline{\theta}}{\partial z}}, \tag{6}$$

where $\overline{\theta}$ is the average potential temperature at height z.

The existence of IGWs in the atmosphere can be visually determined by examining the wave-like characteristics and period (frequency) analysis of meteorological elements such as horizontal and vertical wind speed, temperature, pressure, or their turbulent pulsations (Cava et al., 2019; Roy et al., 2021; Sun, Mahrt, et al., 2015; Wei et al., 2022). Among these variables, IGWs identified through pressure fluctuations are less likely to be contaminated by turbulence (Sun, Nappo, et al., 2015; Wei et al., 2022), making pressure fluctuations the most commonly used atmospheric variable for tracking IGWs. High-resolution pressure fluctuations are influenced not only by instrument high-frequency measurement noise, weather systems, waves, and turbulence but also by semi-diurnal "pressure tides" induced by solar and lunar gravitational forces (Viana et al., 2007). Stull (1988) also noted that the time scale of barometric pulsations associated with IGWs ranged from 1 to 40 min. Therefore, following the method recommended by Wei et al. (2021), we utilize Empirical Mode Decomposition (EMD) to obtain the pressure fluctuation data with time scales less than 45 min. The time scales of IGWs are generally less than 60 min, which is longer than the time scales of turbulent motions. Hence, in Section 3.1, we complement the identification of IGWs by analyzing horizontal wind speed fluctuations after removing trends longer than 60 min, particularly for larger-scale IGWs. However, atmospheric waves often exhibit complex characteristics with varying periods and amplitudes rather than constant periodic and amplitude characteristics. Therefore, wavelet transforms of meteorological turbulence data (U', p') are necessary to verify the presence of IGWs and to obtain their wave energy and frequency.

2.2.5. Methods of Estimating TDR

Different detection methods and data are employed in various ways to estimate the TDR. The near-surface TDR, estimated using the second-order structure function method, is commonly employed in the studies of near-surface atmospheric turbulence structures owing to its stability and low error rates (Bodini et al., 2019; Muñoz-Esparza et al., 2018). According to the recommendation by Muñoz-Esparza et al. (2018), the time interval, τ, is set from 0.1 to 2.0 s, with every near-surface TDR being estimated over a 2 min interval. The TDR is defined as follows:

$$\mathrm{TDR} = \frac{1}{U\tau}\left[\frac{D_u(\tau)}{C_K}\right]^{3/2}, \tag{7}$$

$$D_U(\tau) = <[U(t+\tau) - U(t)]^2>, \tag{8}$$

where $D_U(\tau)$ is the second-order structure function derived from the velocity fluctuation values, U is the mean horizontal wind speed, and C_k is the Kolmogorov constant (≈2.0).

Different remote sensing devices and scanning modes yield varying results in estimating the TDR. Traditional vertical scanning modes, which are limited by detection blind spots, are suitable only for estimating the TDR in middle to upper layers and cannot accurately depict spatial turbulence structures in the lower layers (especially below 400 m). Therefore, this study employs a tilt mode to estimate the TDR in the lower layers (primarily targeting below 500 m), providing a more comprehensive assessment of the turbulence characteristics in the lower atmosphere and compensating for the shortcomings of the vertical scanning mode in lower-level detection. The data reconstruction and extraction methods in the tilt mode are similar to those in the Doppler glide path scanning mode (Chan, 2010). Utilizing the azimuthal structure function effectively reduces the influence of volume-averaging effects (Frehlich & Cornman, 2002). Detailed calculation procedures are described in Frehlich et al. (2006) and Chan (2010). The TDR estimate in tilt mode is defined as follows:

$$\mathrm{TDR} = 0.933668\,\frac{\sigma^3}{L_0}, \tag{9}$$

where σ represents standard deviation of the radial velocity, and L_0 denotes the turbulence scale. Each TDR is estimated over a 2–3 min interval in tilt mode.

3. Results and Discussion

A total of 82 SBL cases with the interaction of LLJ and IGWs and going through regime changes during a whole night, were identified at the ZCIA site in 2022, as shown in Table S2 in Supporting Information S1. While the number may seem limited, these cases are frequent, highly representative of SBL conditions. Due to incomplete data, the number of fully qualified cases was restricted. After considering the strict definitions of LLJ and IGWs, data completeness, the evolution of LLJ-IGWs interactions, and seasonal representativeness, we selected two representative cases for detailed analysis: Case 1 (25 September 2021) representing a strongly SBL, and Case 2 (23 May 2022) representing a weakly SBL. These cases were chosen for their independence and representativeness, reflecting the majority of observed conditions.

3.1. Overview of Cases Featuring the Coexistence of LLJ and IGWs

The FBLTO network enables monitoring of the complete evolution process of LLJ. This study selects two typical cases of LLJ and IGWs interactions for discussion. In Case 1, the LLJ occurred from 22:30 on 25 September 2021, to 06:30 on 26 September 2021 (Figure 2a). The main body of the LLJ appeared within a spatial range of 50–1,000 m above the ground, with jet wind speed maximum ranging from 11 to 16 m/s, and the jet axis height positioned between 300 and 600 m. The LLJ in Case 1 exhibited the characteristics of a low position, long duration (8 hr), and high intensity, during which the jet axis height was sustained, elevated, and declined over time. According to the characteristics of the LLJ and the height variations of its jet axis, the nocturnal period from 19:00 to 07:00 was divided into four stages: (a) before the LLJ (B): 19:00–22:30; (b) stable period (S): 22:30–02:30; (c) rising period (R): 02:30–05:30; and (d) descending period (D): 05:30–07:00. In Case 2, the LLJ occurred from 22:30 on 23 May 2022, to 02:30 on 24 May 2022, as shown in Figure 2b. Compared with Case 1,

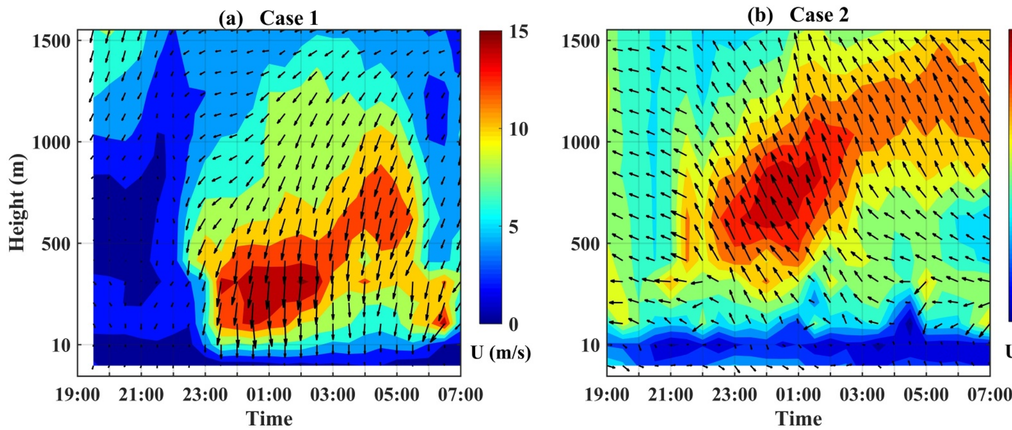

Figure 2. Color shading depicting the variation in the horizontal wind speed with time and height for nocturnal LLJ cases: (a) Case 1: 25 September 2021; (b) Case 2: 23 May 2022. (Color shading represent the horizontal wind speed, arrow directions indicate the horizontal wind direction, and arrow sizes represent the horizontal wind speed magnitude).

the main body of the LLJ in Case 2 appeared at higher altitudes (500–1,100 m), with a shorter duration (4 hr), and lower intensity; the jet wind speed maximum reached 12 m/s, and the jet axis height varied between 600 and 800 m. According to the LLJ occurrence time, the nocturnal period for Case 2 was divided into three stages: (a) before the LLJ (B): 19:00–22:30; (b) persistence of the LLJ (P): 22:30–02:30; and (c) after the LLJ (A): 02:30–07:00.

IGWs were observed in both cases. During period B of Case 1, as shown in Figure 3, the average horizontal wind speed (U) remained low ($U < 1.5$ m/s), while the N_{bv} exhibited extreme values of greater than 0.25 Hz, creating conditions favorable for the occurrence of IGWs. The horizontal wind speed fluctuations (U') were weak and almost negligible, and the wavelet transformed energy density per period and time unit of U' (Figure 3d1) did not exhibit significant wave-like pattern energy peaks. However, the filtered pressure fluctuations (p') showed a single wave with an amplitude of 30 Pa, indicating a weak wave energy zone with an energy peak of 60 Pa^2/s and a wave period of 35 min in the wavelet transform energy density per period and time unit of p' (Figure 3f1). Therefore, IGWs may have been present during period B of Case 1, primarily evidenced by p', as the standard deviations of the atmospheric coherence wave pressure were much greater than those of the turbulent atmospheric pressure, making p' more sensitive for the detection of IGWs (Wei et al., 2022). As period S began, U increased significantly (up to 5.2 m/s), and N_{bv} again exhibited fluctuations greater than 0.25 Hz; both U' and p' exhibited significant wave-like patterns, suggesting the possible presence of IGWs. The wavelet's transforms energy density per period and time unit of both fluctuations (Figures 3d1 and 3f1) displayed significant wave energy peaks of 1.6 m^2/s^3 and 120 Pa^2/s, corresponding to wave periods of 25–30 and 30–40 min, respectively. The corresponding frequencies of waves are 0.21–0.25 s^{-1} for U', 0.16–0.21 s^{-1} for p', both of which are smaller than the N_{bv} (0.26–0.27 s^{-1}) during this period. Furthermore, the time series of horizontal and vertical wind speeds showed an antiphase relationship, as shown in Figure S1 in Supporting Information S1, confirming that the waves observed are indeed IGWs. After 00:30, U gradually decreased, N_{bv} decreased to 0.21 Hz, and the turbulence fluctuations in U' and p' weakened, with significant reductions in wave energy in the wavelet transforming energy density per period and time unit. Therefore, in Case 1, IGWs were observed during the 22:30–00:30 in period S, which was also the period of interaction between the LLJ and IGWs. During periods R and D, U showed a continuous weakening trend from 4.5 to 1.5 m/s overall, while N_{bv} remained stable around 0.22 Hz, the turbulent fluctuation wave amplitudes were weaker than those in period S, and no significant energy peaks were observed in the wavelet transforms. Therefore, IGWs were not observed during periods R and D.

Unlike Case 1, Case 2 exhibited significant wave-like characteristics in the time series of U, N_{bv}, and the turbulent fluctuations (Figure 3, Case 2). In the wavelet transform energy density per period and time unit of U' (Figure 3d2), a wave energy region spanning 20–60 min occurred during 19:00–04:00 discontinuously. The energy peak occurred between 19:00–22:00 (period B), where the wave energy was 0.35 m^2/s^3, and the wave period was 40–60 min. However, in the wavelet transform energy density per period and time unit of p', two energy peaks appeared only during 19:00–02:00, with wave energies of 70 Pa^2/s (90 Pa^2/s), and wave periods of

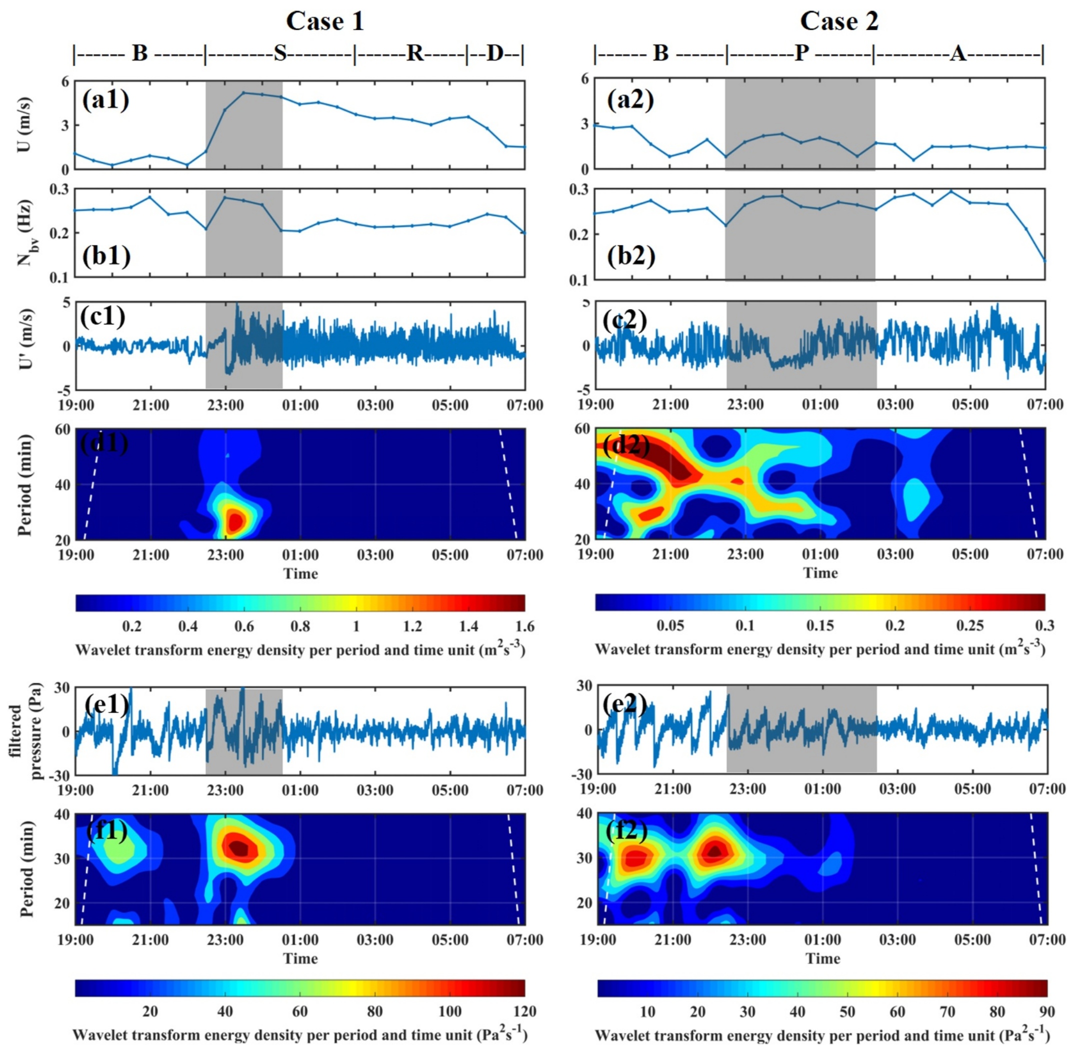

Figure 3. Time series of (a) horizontal wind speed (U), (b) buoyancy frequency (N_{bv}), (c) the horizontal wind speed fluctuations (U'), and (e) the filtered pressure fluctuations (p'). Wavelet transform energy density per period and time unit for (d) the horizontal wind speed fluctuations and (e) the filtered pressure fluctuations. Observational data from eddy covariance system at 2.7 m. (Subscripts 1 and 2 represent Cases 1 and 2, respectively; the shaded areas indicate periods of interaction between LLJ and IGWs.)

28–35 min. The corresponding frequencies of waves are 0.10–0.16 s^{-1} for U', 0.18–0.22 s^{-1} for p', both of which are smaller than the N_{bv} (0.23–0.28 s^{-1}) during this period. Furthermore, the time series of horizontal and vertical wind speeds also show an antiphase relationship, as shown in Figure S2 in Supporting Information S1, confirming that the waves observed are indeed IGWs. Therefore, two scales of IGWs were observed during period B in Case 2.

In summary, we found different characteristics between Case 1 and Case 2: Case 1 featured a lower-position, longer-duration, higher-intensity LLJ interacting with short-duration, strong IGWs, dominated by the LLJ. Case 2 featured a higher-position, shorter-duration, weaker LLJ interacting with long-duration, weaker IGWs, and the long-surviving IGWs played a dominant role, although the IGWs were not as strong as those in Case 1. The subsequent analysis will investigate the evolution mechanism of the SBL turbulence structure caused by the different interactions of LLJ and IGWs by examining the near-surface turbulent intermittency characteristics, spatial turbulence intensity, and coherent structures in both cases.

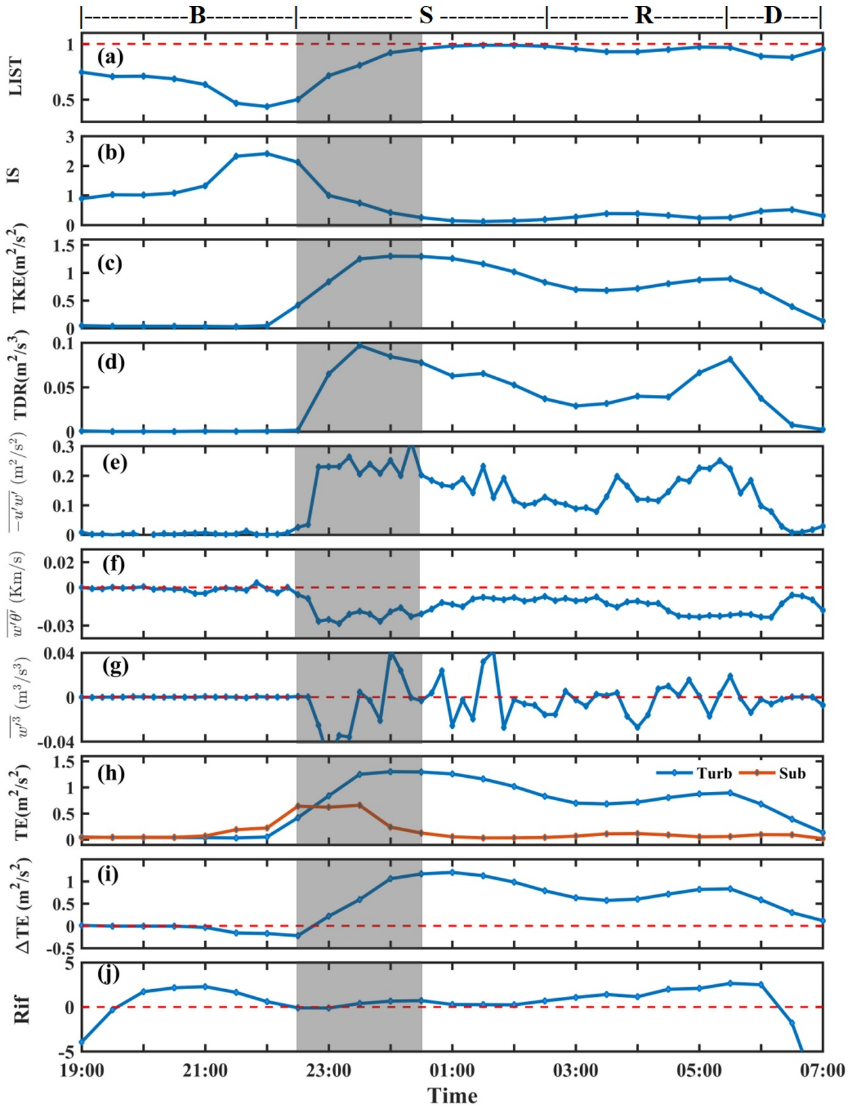

Figure 4. Time series of the (a) near-surface local intermittency strength index (LIST), (b) intermittency strength (IS), (c) turbulent kinetic energy (TKE), (d) turbulent dissipation rate (TDR), (e) momentum flux ($\overline{-u'w'}$), (f) heat flux ($\overline{w'\theta'}$), (g) vertical energy fluxes ($\overline{w'^3}$), (h) total energy of turbulence and sub-mesoscale motion (TTE and STE), (i) difference between the total turbulent energy and total sub-mesoscale energy (ΔTE), and (j) flux Richardson number (R_{if}) for Case 1 in the nocturnal period. Observational data from eddy covariance system at 2.7 m. (The shaded areas indicate periods of interaction between LLJ and IGWs).

3.2. Evolution of the Turbulence Structure in the SBL Dominated by LLJ

Based on the time variations of the near-surface turbulent intermittency intensity indices, LIST and IS, a turbulent intermittency event was detected in Case 1. As shown in Figure 4, during period B of Case 1 (19:00–22:00), LIST decreased from 0.75 to 0.44 (IS increased from 0.9 to 2.4) when the influence of sub-mesoscale motion was prominent and dominant and during the quiescent period of the turbulent intermittent events. During this period, the turbulence intensity was very low, with both TKE and TDR approaching zero, and the momentum flux ($\overline{-u'w'}$), heat flux ($\overline{w'\theta'}$), vertical energy fluxes ($\overline{w'^3}$), and TTE were almost zero. As the sub-mesoscale motion strengthened (with increasing IS), the total sub-mesoscale energy (STE) increased to 0.22 m^2/s^2. The atmospheric stratification was very stable, with R_{if} reaching up to 3.1. Vertically, the TDR was very low below 500 m, approaching zero (Figure 5a), and the vertical spatial mean of TDR gradually changed from significantly lower

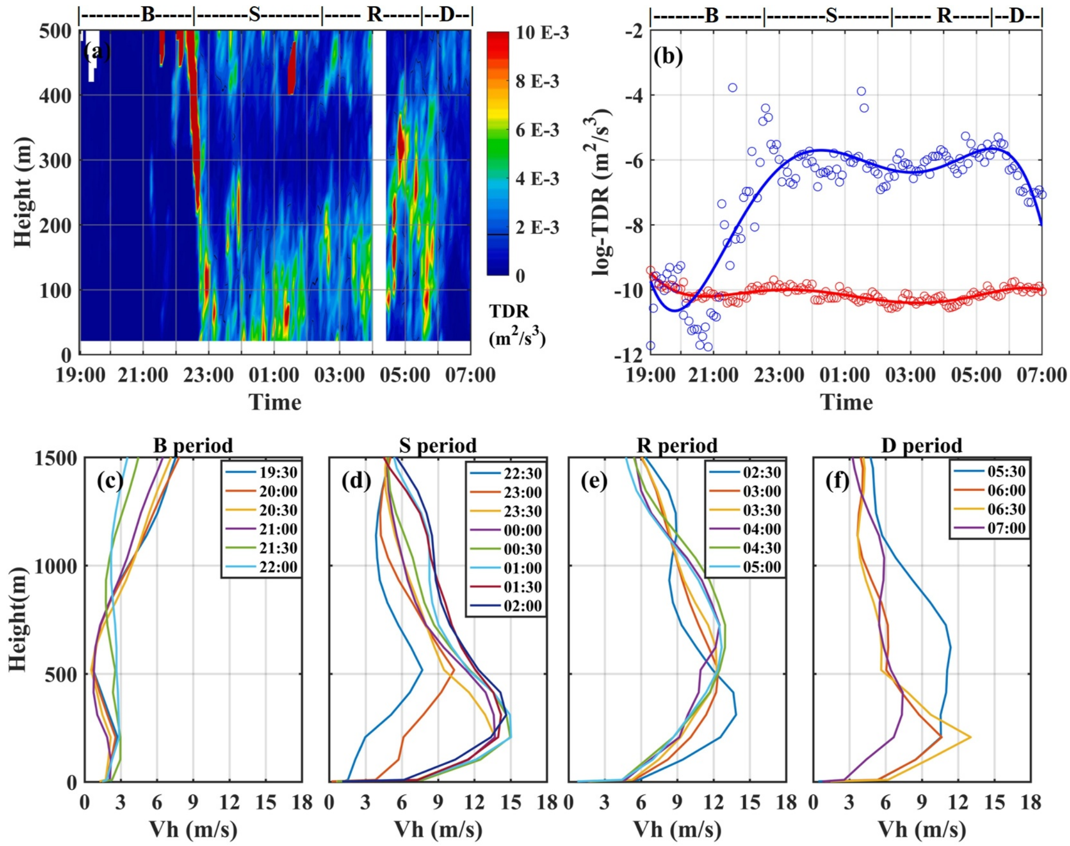

Figure 5. (a) Spatial distribution of the turbulent dissipation rate (TDR) in the nocturnal period for Case 1; (b) time series of the spatially averaged TDR between 60 and 500 m (circles represent actual values, curves represent the best fit, blue represents Case 1, and red represents the monthly average at each time) and wind profile diagrams for the four periods of Case 1: (c) period B, (d) period S, (e) period R, and (f) period D.

than the month's average to greater than the month's average (Figure 5b). Meanwhile, the wind profiles during this period exhibited low wind speeds throughout the layer, mostly below 4.0 m/s (Figure 5c). The surface winds were always lower than 1.5 m/s and belong to regime 1, typified by weak winds and strong stability, in the classification of Sun et al. (2012, 2016).

During the transition between periods B and S, the LIST increased (IS weakened), and turbulent intermittency events erupted. Between 22:00 and 23:30, the STE reached a maximum of 0.66 m^2/s^2 as the IGWs wave energy peaked, and the TTE also increased to 1.25 m^2/s^2 (Figure 4h). The TKE (TDR) also significantly rose to 1.30 m^2/s^2 (0.10 m^2/s^3). Moreover, the difference in energy between TTE and STE (ΔTE = TTE − STE) rapidly increased from negative values to 0.64 m^2/s^2, indicating a significant enhancement in the momentum and heat fluxes. The turbulent energy vertical transport was −0.148 m^3/s^3, owing to the growth of the KE of the turbulent motion, indicating a downward energy transfer during this period. Correspondingly, during this period, a significant energy transfer occurred within the 100–500 m range based on Lidar observations (Figure 5a). From the wind profile changes (Figure 5d), the jet axis height decreased from 500 to 250 m, and strong wind shear below 500 m was observed at 22:30 and 23:00. The surface wind speeds increased from 1.2 m/s (22:30) to 4.0 m/s (23:00) which exceeds the threshold wind speed (2.0 m/s, see in Figure S3 in Supporting Information S1) determined by HOST pattern in Sun et al. (2012, 2016). At this time, the atmospheric stratification stability decreased significantly and the boundary layer stability transitioned from strong to weak. Analysis of the near-surface and spatial turbulent structures revealed that the LLJ generated at this time was a local boundary layer LLJ which caused downward energy transfer and surface wind speeds enhancement. This turbulent intermittency event is triggered by the interaction between wind shear and stable stratification in a strongly SBL, known as the internal factor of intermittent turbulence occurrence (Allouche et al., 2022), also belongs to the A type intermittency caused by the surface wind speeds enhancement in HOST pattern of Sun et al. (2012, 2016). Simultaneously, the wave energy of

IGWs increased and STE grew. Observational studies by Mortarini et al. (2018) found that the Kelvin-Helmholtz instability induced by strong wind shear at the LLJ nose and the ascent of cold air could generate IGWs. The peak of the IGWs wave energy observed at the near-surface may be due to the downward propagation of IGWs or related to wave decay and intermittent turbulence. The appearance of LLJ may lead to strong non-stationarity, thereby increasing the energy of the sub-mesoscale motion.

During period S from 23:30 to 00:30, the LIST (IS) gradually tended toward 1 (0), and the influence of the sub-mesoscale motion faded. The TKE slightly increased to a peak of 1.32 m^2/s^2, while the TDR decreased slightly to 0.08 m^2/s^3. The STE decreased from its peak to 0.13 m^2/s^2, corresponding to the weakening of the IGWs wave energy. The TTE increased slightly to a peak of 1.30 m^2/s^2. It is hypothesized that energy conversion from sub-mesoscale motion to turbulent motion occurred during this period, with ΔTE continuing to increase from −0.15 to 0.28 m^2/s^2. During this process, the momentum and heat fluxes remained strong; however, $\overline{w'^3}$ indicates that energy was alternately transferred upward and downward. The wind profile changes show that from 23:30 to 00:30 (Figure 5d), the jet axis height remains constant, while jet wind speed maximum increases and exceeds 12 m/s. Meanwhile, the wind shear above and below the LLJ nose continued to intensify. The surface wind speed remains around 5.0 m/s and with large wind shear which means the surface layer belongs to regime 2 in HOST of Sun et al. (2012, 2016). Figure 5a shows that the turbulent energy was concentrated below 100 m. The near-surface and spatial turbulent structures reveal that the continuous intermittent turbulence burst during this period was driven by the near-surface strong wind shear and energy conversion from sub-mesoscale motion. In strongly SBL, turbulent intermittency events driven by the interaction between wind shear and stable stratification are often periodic, as confirmed by large-eddy simulation experiments (Van der Linden et al., 2020). However, previous studies have emphasized that this periodic feedback is difficult to observe in mid-latitude atmospheric boundary layers owing to the influence of sub-mesoscale motion. This was directly evidenced by field observations in this study. From 00:30 to 02:00, as the sub-mesoscale motion energy was depleted the near-surface layer exhibited purely turbulent motion with a strong momentum flux and stable heat flux. However, this period was solely energized by the near-surface wind shear, resulting in lower turbulent transport and energy compared with the previous period. Spatially, from 01:00 to 02:00, the maximum wind speed and position of the LLJ remained stable, and turbulent energy was almost always present below 100 m, indicating strong turbulence throughout the layer.

Throughout period S the LLJ evolved from appearance (22:30–23:00), through development (23:30–00:30), and to stabilization (01:00–02:00). Changes in the surface turbulent characteristic parameters indicate that energy transfer during 22:30–23:00 triggered the LLJ and provided energy for the outbreak of turbulent intermittency events, whereas wind shear generated by the LLJ simultaneously induced IGWs. During the subsequent 23:30–00:30 period, the energy conversion between the IGWs and the turbulent motion and strong near-surface wind shear jointly sustained an intermittent turbulence burst. After the dissipation of the IGWs (01:00–02:00), influenced by the LLJ solely, the near-surface layer exhibited purely turbulent conditions. The average turbulent transport for these three periods were 0.087 m^2/s^2 for $\overline{-u'w'}$, −0.016 Km/s for $\overline{w'\theta'}$, −0.021 m^3/s^3 for $\overline{w'^3}$; 0.232 m^2/s^2 for $\overline{-u'w'}$, −0.021 Km/s for $\overline{w'\theta'}$, and 0.006 m^3/s^3 for $\overline{w'^3}$; in the subsequent purely turbulent stage, the values were 0.116 m^2/s^2 for $\overline{-u'w'}$, −0.010 Km/s for $\overline{w'\theta'}$, and −0.001 m^3/s^3 for $\overline{w'^3}$. It is evident that the intense intermittent turbulence burst process resulted in stronger material and energy transport compared with purely turbulent transport. The spatial distribution of the turbulence intensity (Figure 5b) shows that the TDR first increased and then decreased, corresponding to the surface turbulence characteristic results, but it remained significantly higher than the monthly average. Figure 5d shows that during the development and stabilization of the LLJ (23:30–02:00), the lower boundary of the LLJ could dropped to as low as 100 m, where intense turbulent mixing at the near-surface reduced the mean field gradient, causing the LLJ to lift.

In period R (02:30–05:00), as the jet axis height lifted from 300 to 700 m and jet wind speed maximum decreased from 14 to 12 m/s, the influence of the LLJ on the near-surface weakened. The high TDR region gradually rose above 100 m (Figure 5a), and the turbulence intensity below 100 m was significantly lower than that during period S. The average TDR for the entire layer was lower than during the intermittent turbulence burst period but still remains high (Figure 5b). Although the near-surface wind speed has been decreasing, it remains greater than 2.0 m/s, meaning the near-surface is still in regime 2 of the HOST pattern. The generation of large turbulent eddies by bulk wind shear between observation heights and the ground surface controls the surface layer. The changes in the near-surface LIST and IS also indicated that period R was predominantly turbulent. The R_{if}

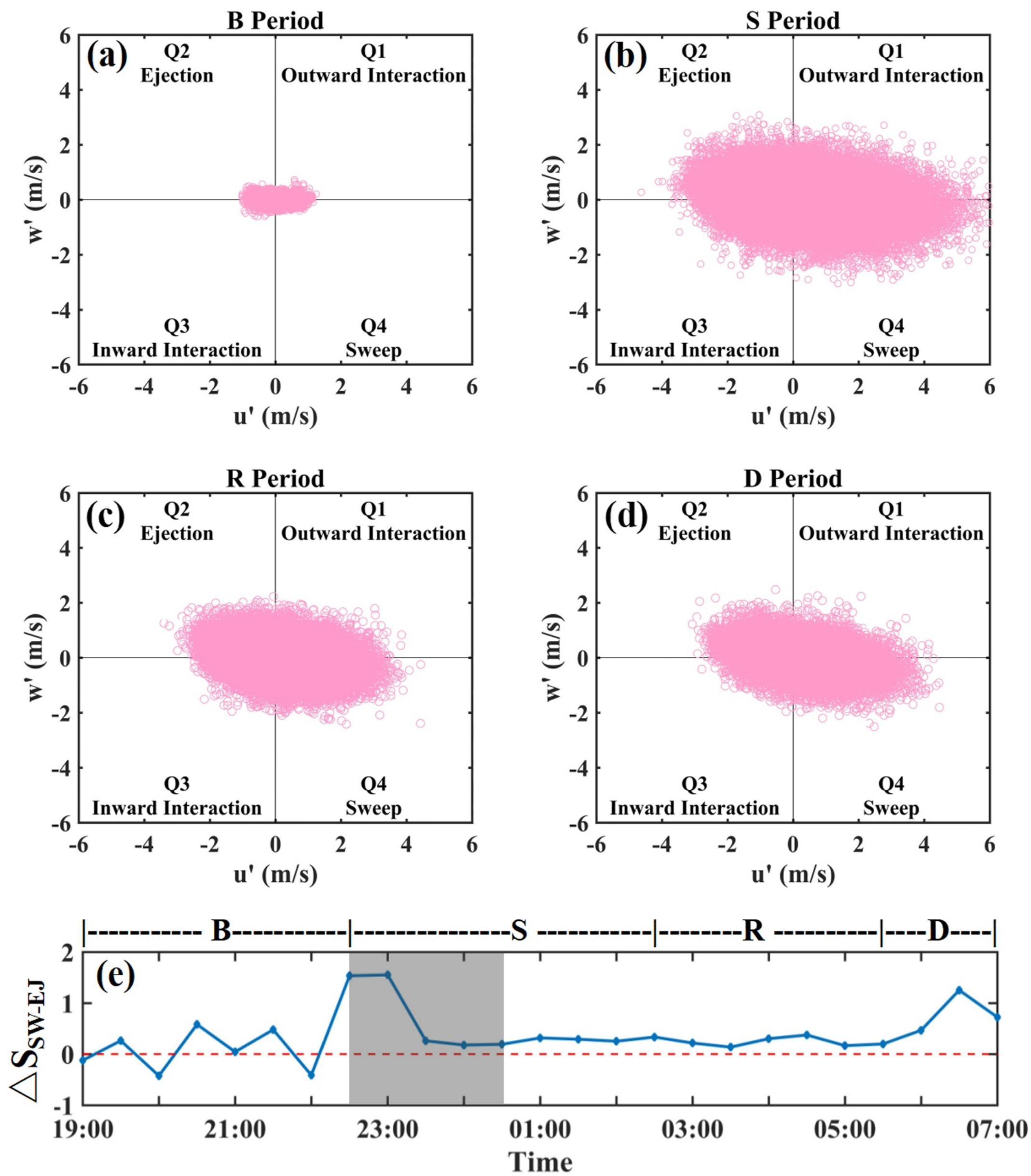

Figure 6. Scatter plots of the u' and w' components in the four quadrants during different periods of Case 1 in the nocturnal period: (a) period B, (b) period S, (c) period R, and (d) period D; (e) time series of the flux contribution difference of updrafts and downdrafts, $\Delta S_{SW\text{-}EJ}$. (The shaded areas indicate periods of interaction between LLJ and IGWs).

gradually increased, and the atmospheric stability gradually strengthened. During the period D (05:30–06:00), as shown in Figure 5f, the jet axis height decreased from 600 to 200 m, corresponding to a downward energy transfer below 100 m (Figure 5a). However, at this time, the R_{if} at the near-surface is relatively high, reaching 2.5, indicating a strongly stable near-surface state. Simultaneously, with a decrease (increase) in LIST (IS), the turbulent flux, turbulent energy, and vertical turbulent energy transport decreased significantly. It is speculated that the lifting of the LLJ gradually reduced its influence on the near-surface, returning the nocturnal boundary layer to a strongly stable state. Meanwhile, an increase in the vertical mean gradient further caused the lower boundary of the LLJ to drop. However, the spatial turbulence intensity during this period was not as strong as that during period S (Figure 5a), and the spatial average TDR rapidly decreased, preventing the near-surface from triggering another intermittent turbulence burst.

To further analyze the evolution of near-surface turbulent structures under the interaction between LLJ and IGWs in Case 1, we discuss the coherent structures of the turbulence during different periods. As shown in Figure 6a, during period B, the turbulent fluctuations were small in the strongly SBL, with u' and w' concentrated in the range of −1 to 1 m/s. Updraft and downdraft motions alternated, and the flux contribution difference of the updrafts and downdrafts, $\Delta S_{SW\text{-}EJ}$, fluctuated around zero. During period S, an intermittent turbulence burst occurred because of the interaction between the LLJ and IGWs. The turbulent fluctuations were strong, with u' increasing significantly from (−1, 1) to (−5, 6) m/s and w' from (−1, 1) to (−3, 3) m/s. The turbulence was notably enhanced, and the points in each quadrant became more dispersed compared to period B, with downdrafts dominating, and the $\Delta S_{SW\text{-}EJ}$ reached 1.55. In period R, as the LLJ lifted, the near-surface turbulent fluctuations were weaker than during period S, with u' ranging from −4 to 4 m/s and w' ranging from −2 to 2 m/s, still dominated by downdrafts; however, $\Delta S_{SW\text{-}EJ}$ decreased to around 0.2. During period D, as the LLJ descended, the near-surface turbulent fluctuations increased again, with u' and w' dispersing more than during period R and remaining dominated by downdrafts. The changes in the turbulent coherent structures and fluctuations during different periods are consistent with the above turbulence characteristic analysis.

3.3. Evolution of the Turbulence Structure in the SBL Dominated by IGWs

In Case 2, because of the continuous influence of the IGWs, the near-surface signals were persistently affected by sub-mesoscale motions, and the vertical spatial values of the TDR (blue solid line in Figure 8b) has significantly fluctuated. The time series of LIST and IS at the near-surface indicated two turbulent intermittency events occurring in periods B and A, as shown in Figure 7. From 19:00 to 21:00 in period B, the quiescent period of the first turbulent intermittency event occurred. The energy of the IGWs observed at the near-surface was relatively strong (Figures 3d2 and 3f2), with LIST decreasing from 0.86 to 0.55 (IS increasing from 0.60 to 1.56). The momentum flux, heat flux, and energy transport decreased significantly, with TTE decreasing from 0.86 m^2/s^2 to 0.13 m^2/s^2. STE (0.29 m^2/s^2) was slightly greater than TTE (0.13 m^2/s^2), and ΔTE decreased from 0.52 to −0.16 m^2/s^2. The atmospheric stability was significant, with a maximum R_{if} value of 0.33. Compared to period B in Case 1, period B in Case 2 was weakly stable. The wind profile (Figure 8c) shows that the jet axis height rose from 500 to 1,000 m, jet wind speed maximum exceeded 6 m/s, and the wind speed below 500 m was significantly higher than that in Case 1. Correspondingly, Figure 8a shows that the spatial turbulence intensity was stronger than that in period B in Case 1. Thus, period B in Case 2 can be considered a weak SBL.

From 21:00 to 00:00, the first turbulent intermittency event entered a burst period, with LIST increasing from 0.55 to 0.87 (IS decreasing from 1.56 to 0.56). The momentum flux, heat flux, and energy transport also increased. During this period, TTE continued to increase, but STE decreased slightly between 21:00 and 22:00 without completely disappearing. This corresponds to the energy variation in the IGWs shown in Figure 3 for Case 2. At 21:00, the energy of the small-scale IGWs decreased, indicating a conversion of sub-mesoscale motion energy to turbulent energy, with ΔTE increasing from −0.16 to 0 m^2/s^2. The energy of large-scale IGWs remains at its peak at this moment. At 22:00, another peak in the energy of small-scale IGWs was observed, accompanied by a decrease in the energy of large-scale IGWs. This may indicate an energy transfer between small- and large-scale IGWs at this time. Mahrt (2014) suggested the existence of an inverse-scale energy transfer. By 00:00, the energy of the small-scale IGWs had significantly weakened and nearly dissipated, corresponding to a decrease in the STE to 0.14 m^2/s^2. From 21:00 to 22:00, Figure 8a shows very weak turbulence intensity below 500 m, indicating that this burst period was unrelated to vertical spatial turbulence and was driven solely by sub-mesoscale motions in the near-surface. At 22:30, the wind profile shows that the jet axis height was 600 m and jet wind speed maximum was less than 10 m/s, with increased shear below 500 m. The spatial distribution of the TDR also indicates high values between 300 and 500 m. The jet wind speed maximum exceeded 10 m/s at 23:00, indicating the presence of an LLJ after 22:30. The near-surface TTE exceeded the STE after 22:30. From 22:00 to 23:00, the turbulence intensity fluctuations increased throughout the vertical space, significantly exceeding the monthly average after 22:30, as shown in Figure 8b. From 23:00 to 00:00, the LLJ persisted, and the turbulence intensity remained high below 300 m. In summary, this intermittent burst was initially induced by sub-mesoscale motion energy conversion (IGWs energy breaking) and possibly involved energy transfer between small- and large-scale IGWs. That is, energy exchange occurred between different scales of sub-mesoscale motions without fully transferring to turbulent scales. Subsequently, the combined effects of sub-mesoscale motion energy conversion and the LLJ sustained an intermittent turbulence burst. The average turbulent transport during these two stages was 0.034 m^2/s^2 for $\overline{-u'w'}$, −0.016 Km/s for $\overline{w'\theta'}$, and −0.001 m^3/s^3 for $\overline{w'^3}$ in the first stage, and 0.057 m^2/s^2 for $\overline{-u'w'}$,

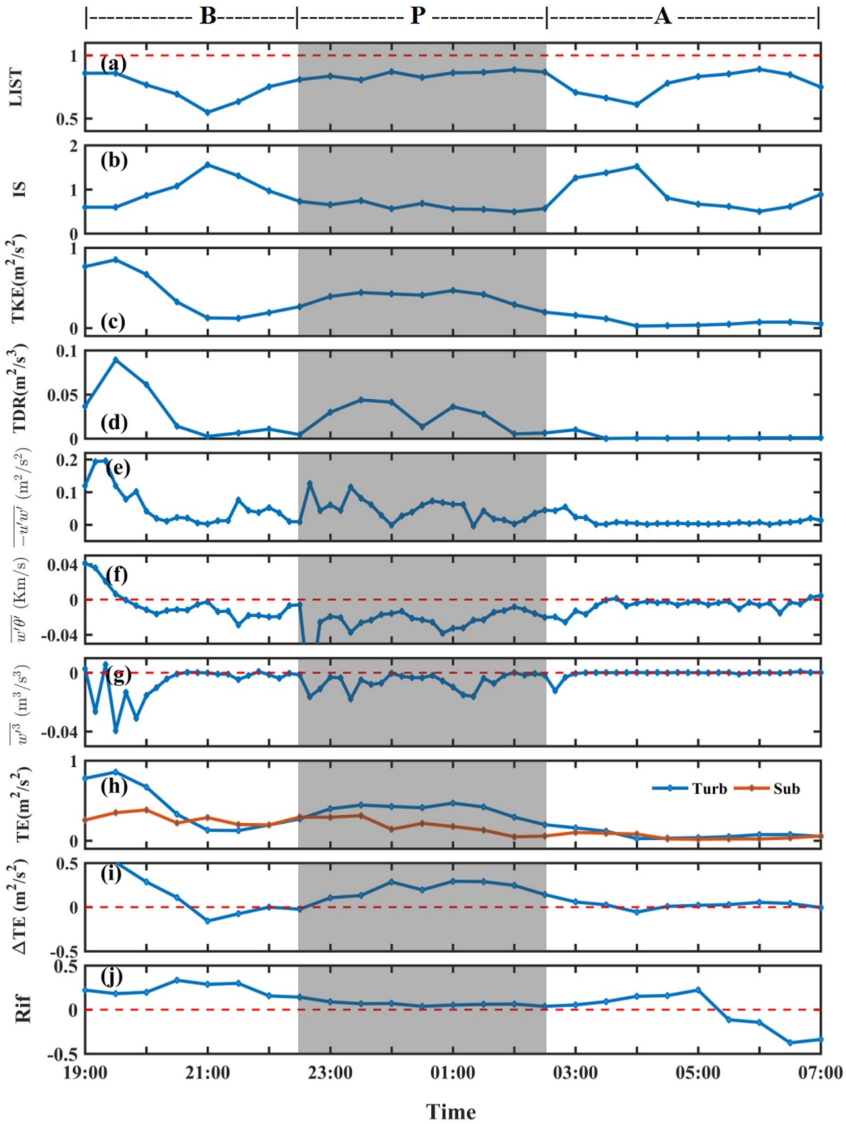

Figure 7. Time series of the (a) near-surface local intermittency strength index (LIST), (b) intermittency strength (IS), (c) turbulent kinetic energy (TKE), (d) turbulent dissipation rate (TDR), (e) momentum flux ($\overline{-u'w'}$), (f) heat flux ($\overline{w'\theta'}$), (g) vertical energy transport ($\overline{w'^3}$), (h) total energy of turbulence and sub-mesoscale motion (TTE and STE), (i) difference between the total turbulent energy and total sub-mesoscale energy (ΔTE), and (j) flux Richardson number (R_{if}) for Case 2 in the nocturnal period. Observational data from eddy covariance system at 2.7 m. (The shaded areas indicate periods of interaction between LLJ and IGWs).

-0.030 Km/s for $\overline{w'\theta'}$, and -0.007 m^3/s^3 for $\overline{w'^3}$ in the second stage. The turbulent transport in the stage influenced solely by sub-mesoscale motion was significantly weaker than that in the stage influenced by the interaction between sub-mesoscale motion and the LLJ.

During the early part of period P (22:30–00:00), the jet axis height changed from 600 to 700 m, and the jet wind speed maximum ranged from 10 to 11 m/s. The edge of the wind shear below the LLJ reached approximately 300 m, with TDR indicating strong turbulence intensity below 300 m and intermittent turbulence burst in the near-surface. This turbulent mixing process reduced the mean field gradient, causing the jet axis height to increase. During the late part of period P (00:00–02:30), the jet axis height lifted above 800 m, reducing the impact of the LLJ on the surface. The TDR values below 300 m significantly decreased and exhibited a discontinuous distribution over time, with high TDR regions gradually appearing above 300 m. During this time, the near-surface LIST remained at 0.87, and the IS remained at approximately 0.5. Small-scale IGWs had a slight impact, while the

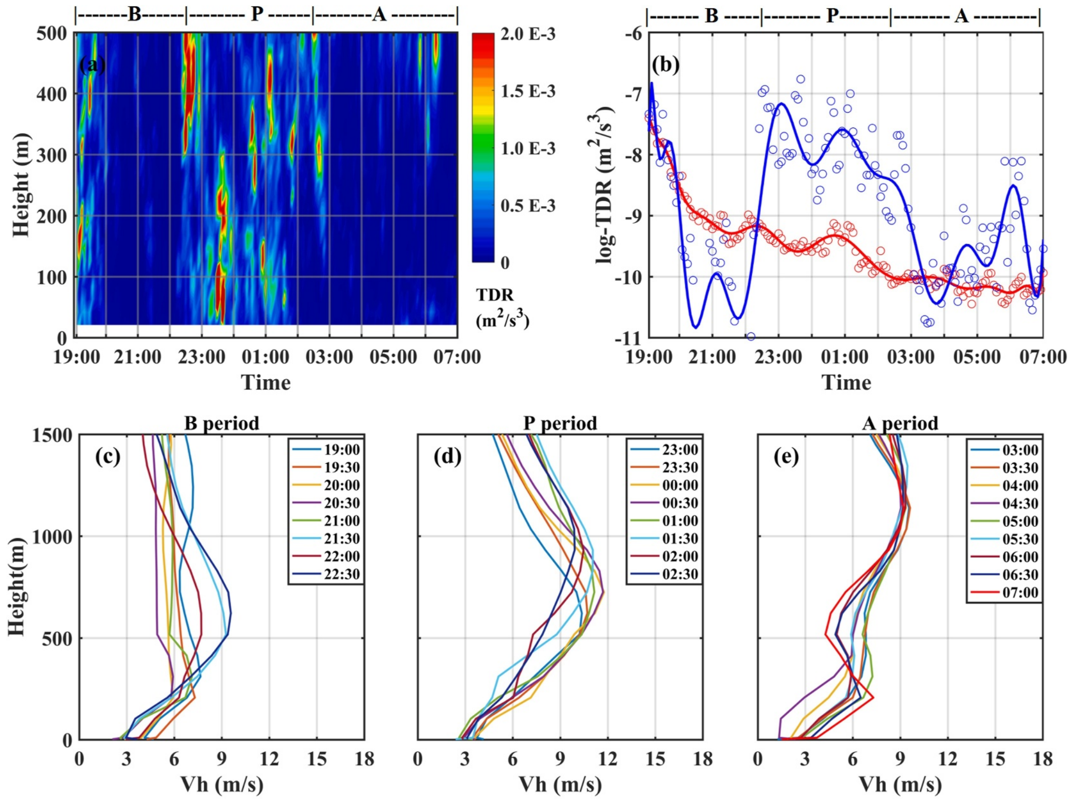

Figure 8. (a) Spatial distribution of turbulent dissipation rate (TDR) in the nocturnal period for Case 2; (b) time series of the spatially averaged TDR between 60 and 500 m (circles represent actual values, curves represent best fit, blue represents Case 2, and red represents the monthly average at each time) and wind profiles diagrams for the three periods of Case 2: (c) period B, (d) period P, and (e) period A.

energy of large-scale IGWs weakened. However, at the near-surface, turbulence was the dominant motion, with TTE (0.47 m^2/s^2) exceeding STE (0.18 m^2/s^2), and R_{if} approaching zero. The near-surface stability transitioned from weakly stable to nearly neutral. From 21:00 to 00:00, on one hand, the IGWs energy dissipated through conversion between different scales of motion; on the other hand, the sustained intermittent turbulence burst driven by the LLJ reduced the near-surface stability, possibly hindering the IGWs propagation.

In period A (02:30–04:00), the jet axis height gradually ascended from 1,000 to 1,200 m, then dissipated, and the influence of small-scale IGWs completely vanished; however, the impact of large-scale IGWs persisted. The signals of sub-mesoscale motion were still detectable at the near-surface. This marked the quiescent period of the second turbulent intermittency event, with near-surface atmospheric stability recovering to weakly stable, and the R_{if} gradually increasing from zero. Below 500 m, the TDR decreased to nearly zero, indicating that the entire layer of the atmosphere returned to a weakly turbulent and stable state. As the large-scale IGWs completely disappeared, the time series of LIST and IS show the burst period of the turbulent intermittency event (04:00–06:00). However, owing to the larger scale of the IGWs in the second turbulent intermittency event, the energy was significantly weaker than that in the first turbulent intermittent event, and there was no significant energy conversion between sub-mesoscale and turbulent motions, with ΔTE close to zero, and no significant enhancement in the turbulent transport or energy. From 06:00 to 07:00, the spatial distribution of the TDR showed very low values throughout the layer, with the near-surface turbulent flux and intensity both being very small.

To further analyze the evolution of the near-surface turbulence structure under the interaction of the LLJ and IGWs in Case 2, we discuss the turbulent coherent structures during different periods. As shown in Figure 9a, during the early part of period B, the turbulence fluctuations were small in the weakly SBL, with u' and w' concentrated in the range of −2 to 3 m/s and −2 to 2 m/s, respectively, dominated by downdrafts, with $\Delta S_{SW\text{-}EJ}$ peaking at 1.4. During the BP burst period, intermittent turbulence burst was induced by the interaction of LLJ and IGWs, accompanied by strong turbulence fluctuations, with u' increasing from (−2, 3) to (−3,4) m/s, while w'

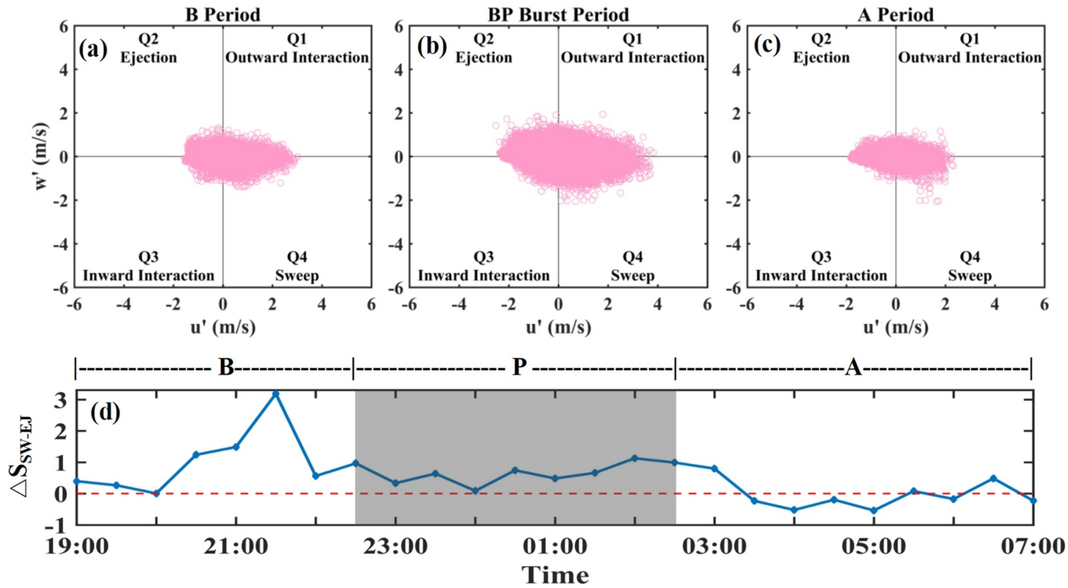

Figure 9. Scatter plots of the u' and w' components in the four quadrants during different periods of Case 2 in the nocturnal period: (a) period B, (b) BP burst, and (c) period A; (d) time series of the flux contribution difference of updrafts and downdrafts, $\Delta S_{SW\text{-}EJ}$. (The shaded areas indicate periods of interaction between LLJ and IGWs).

remained within −2 to 2 m/s. Compared to the other two periods, the points in each quadrant during the BP burst period were more dispersed, though not as much as in Case 1. This period was dominated by downdrafts, with $\Delta S_{SW\text{-}EJ}$ peaking at 3.2. In period A, the ascent of the LLJ reduced the near-surface turbulence fluctuations compared to those in the BP burst period, with u' and w' more concentrated in the range of −2 to 2 m/s. The dominant motion of near-surface turbulence coherent structures changed from downdrafts to updrafts, with $\Delta S_{SW\text{-}EJ}$ decreasing to negative values. Similarly, the changes in turbulence coherent structures and turbulence fluctuations in Case 2 are consistent with the turbulence characteristics analysis.

3.4. Discussion on the Interaction Between LLJ and IGWs in the SBL

Through more than a year of continuous observations, two typical SBL evolution processes were identified, characterized by turbulence intermittency driven by the interaction between LLJs and IGWs. The analysis presented above details each process. Here, we focus on discussing how LLJs and IGWs interact with each other.

Existing literature has found that LLJs or strong shear instability related to LLJs may generate IGWs (Fitzjarrald & Moore, 1990; Luo & Fritts, 1993; Sun et al., 2004). In fact, the formation of LLJs in a very SBL is closely related to the internal factors (the interaction between wind shear and atmospheric stratification stability) of turbulence intermittency as suggested in Businger (1973). Because of the strong radiative cooling of the underlying surface and the convergence and divergence of momentum flux at certain altitudes, very stable boundary layers can exhibit jet-like maxima in wind speed profiles. Banta et al. (2007) demonstrated similar characteristics in the vertical structure of very stable boundary layers: a shallow traditional boundary layer with weak intermittent turbulence; above this shallow boundary layer sat a layer of very weak turbulence and negligible turbulent mixing, like a quiescent layer; and the atmosphere above which may include the remnants of the previous afternoon's mixed layer and the free atmosphere, most likely consists of many layers itself, at least some having intermittent turbulence. Mortarini et al. (2018) further confirmed the layered SBL structure and found that gravity waves were formed in the quiescent layer and propagated both upward and downward, triggering intermittent turbulent bursts outside the quiescent layer. In this study, observations show that between 23:00 and 23:30 in Case 1, the LLJ nose region descended significantly from 500 m to below 300 m, while intermittent turbulence events and IGWs were detected at the near-surface. Two possible explanations exist for the generation of IGWs at this time. First, IGWs may have always existed in the upper regions of the very SBL but were gradually pushed downward as the laminar layer was engulfed by the turbulent layer accompanying the formation of the local LLJ.

This compression could have caused IGWs to be detected at the near-surface. Second, the IGWs could be related to the quiescent layer near the LLJ nose region, as demonstrated by Mortarini et al. (2018).

In this case, IGWs formed in the quiescent layer, propagated downward to the surface, and broke at the ground. More intensive vertical turbulence observations are needed to determine the exact cause. In summary, the generation of IGWs in Case 1 is closely related to the formation of the LLJ in a very SBL. The intermittent turbulence events in Case 1 were primarily triggered by the internal feedback mechanism proposed by Businger (1973), representing a process primarily dominated by internal factors of turbulence intermittency. Throughout this process, the very SBL transitioned into a weakly SBL due to the effects of turbulence intermittency bursts, and the presence of IGWs was short-lived.

While existing studies on the impact of IGWs on LLJs are relatively limited. Sun et al. (2004) found that turbulence intermittency events caused by solitary wave and IGWs, during a night with a 7 m s^{-1} jet, triggered significant downward transport of momentum flux, leading to momentum flux convergence and the formation of a local wind maximum or jet. Corrêa et al. (2021) analyzed one dynamically night that included three distinct periods: a weakly SBL characterized by coherent turbulence structures generated at the canopy top; an orographic GW above the roughness sublayer suppressed coherent structure and strongly influenced the boundary layer structure both above and below the canopy; and a period with low turbulence intensity at the canopy top that allowed the development of an LLJ. In the Case 2 of this study, the wave-like characteristics observed in the spatial TDR data suggest that IGWs likely existed throughout the entire SBL before the LLJ appeared. Near-surface observations show that IGWs continuously triggered intermittent turbulence events. Within the vertical structure of the SBL, IGWs may have influenced momentum transport, as discussed by Sun et al. (2004) and Corrêa et al. (2021), thereby contributing to the formation of the LLJ. Furthermore, both cases in this study indicate that the occurrence of intermittent turbulence bursts enhanced near-surface turbulence mixing, reduced gradients, and decreased atmospheric stratification stability, potentially causing the LLJ to rise. Additionally, the energy transfer between sub-mesoscale motions and turbulent motions also contributed to the dissipation of IGWs. In summary, in Case 2, IGWs, as a sub-mesoscale motion, persisted longer compared to Case 1, driving intermittent turbulence events even before the appearance of the LLJ and likely contributing to its formation. Therefore, Case 2 can be considered a process dominated by external factors of turbulence intermittency.

This study, based on the detection and quantitative characterization of turbulence intermittency, clearly demonstrates the occurrence, development, and dissipation of turbulence intermittency events dominated by LLJ and IGWs, respectively. The two typical SBL evolution processes selected in this study represent processes dominated by internal and external factors of turbulence intermittency, respectively. The analysis demonstrates how LLJs generate intermittent turbulence and activate IGWs, discussing how internal SBL factors can trigger external factors, as shown in Case 1. It also analyzes how external disturbances alter vertical mixing, thereby changing the regimes of the SBL, as in the case of Case 2. While previous studies were limited to near-surface layers or very shallow boundary layers, the results of this study provide new insights into the evolution of the entire boundary layer. However, the onset and evolution of atmospheric disturbances in the SBL are highly complex, and to fully understand the interaction between LLJ and IGWs, dense regional and vertical turbulent observations are necessary to clarify the underlying physical details.

4. Conclusion

In the SBL, different scales of motion are intertwined, and the vertical structure is highly localized, making it challenging to predict transitions between strongly and weakly turbulent states. This study utilized the FBLTO network at the Atmospheric Physics and Atmospheric Environment Continuous Observation Station at Lanzhou Zhongchuan International Airport, China. The network includes ground turbulence observations using the eddy covariance system and vertical-space turbulence observations using Lidar. The FBLTDPS was developed to include data preprocessing, wind data fusion, and TDR estimation from the sonic anemometer and Lidar. This study focused on studying the mechanisms by which the interaction between LLJ and IGWs affects the evolution of the SBL structure. In this paper, two individual cases are selected. Case 1 represents a strongly SBL characterized by a lower-position, longer-duration, and stronger LLJ interacting with short-duration, stronger IGWs, where LLJ plays a dominant role; whereas Case 2 represents a weakly SBL characterized by a higher-position, shorter-duration, and weaker LLJ interacting with long-duration and weaker IGWs, where IGWs play a dominant

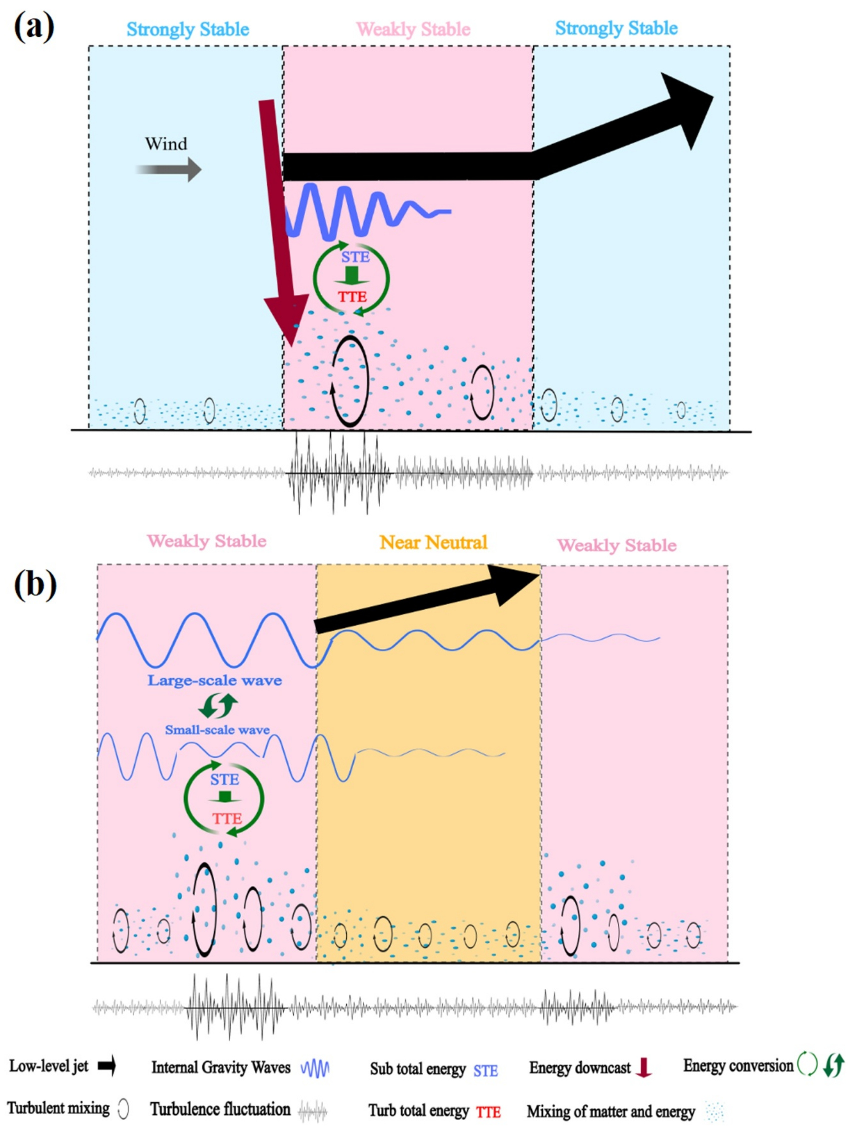

Figure 10. Schematic representation of the interaction of LLJ and IGWs in (a) the strongly stabilized boundary layer and (b) the weakly stabilized boundary layer affecting the evolution mechanism of the turbulent structure of the stable boundary layer.

role. Figure 10 summarizes the mechanisms by which the interactions between the LLJ and IGWs affect the evolution of the SBL turbulence structure in both strongly and weakly SBL conditions.

After maintaining a strongly SBL for a relatively long time (nearly 4 hr), as shown in Figure 10a, a strong downward energy transfer occurred at a height of 500 m, producing strong wind shear, enhancing the near surface wind speed exceeding threshold value determined by HOST that drove an intermittent burst of near-surface turbulence and induced IGWs. Subsequently, the sub-mesoscale motion energy gradually dissipated and was converted into turbulence energy, sustaining the intermittent turbulence burst. The near-surface material and energy transport, as well as the turbulence intensity, were significantly enhanced during this process. As the sub-mesoscale motion energy was exhausted and the LLJ stabilized, the near-surface motion became predominantly turbulent dominated by large turbulent eddies by bulk wind shear between observation heights and the ground surface. During this process, the boundary layer transformed from a strongly stable state to a weakly stable state. In the vertical space, the turbulence intensity below 100 m was strong, leading to uniform mixing of material and energy below 100 m and reducing the mean field gradient, producing a gradual rise of the LLJ. As the LLJ rose, its influence on the near-surface weakened, restoring the boundary layer to a strongly stable state. Sub-mesoscale motion was again present and was detected in the signals collected in the near-surface layer, resulting in a significant weakening of the near-surface layer turbulent transport, and turbulence intensity, compared to the burst period. Over time, the turbulence intensity below 100 m significantly weakened (especially below 50 m), and the mean field gradient was reestablished, causing the LLJ to descend again. However, the descending LLJ did not break the strong SBL state, and no further intermittent turbulence burst occurred at the near-surface.

In the weakly SBL (Figure 10b), IGWs are already present at the near-surface. Driven by sub-mesoscale motion energy conversion (IGWs wave energy breaking), an intermittent turbulence burst occurred at the near-surface. Simultaneously, possible energy exchanges between small- and large-scale IGWs occurred, with energy being exchanged between different scales of sub-mesoscale motions without fully transferring to turbulence scales. Thus, the burst intensity of this turbulent intermittency event was not as strong as that in the strong SBL. However, the subsequent emergence of the LLJ sustained this turbulent intermittent outburst event and contributed to a decrease in near-surface stability, which may also have hindered the propagation of IGWs. Then, as the LLJ rose, the entire atmosphere returned to a weakly turbulent and weakly stable state. Throughout the case of weakly SBL, owing to the dominant role of the long-term sustained IGWs, both the near-surface and spatially averaged turbulence characteristics exhibited certain fluctuations.

Relying on the FBLTO network, this study clarifies the interaction mechanism between the internal and external factors of turbulent intermittency through the analysis of two typical cases. In addition, the energy conversion of motions on different scales is clarified, and the state transition and structural evolution mechanism of both strongly stable and weakly SBLs are elucidated. The results of this study are important for advancing theoretical research and simulation developments of the SBL.

Conflict of Interest

The authors declare no conflicts of interest relevant to this study.

Data Availability Statement

Data used in this study are available via Ding and Ren (2024, https://doi.org/10.6084/m9.figshare.26413861.v1).

Acknowledgments

The authors sincerely appreciate the valuable suggestions provided by the three anonymous reviewers on a previous version of the manuscript. This work was jointly funded by grant from National Natural Science Foundation of China (42475184, 42305071, 42090031, 42175092), the National Key Research and Development Program of China (2023YFC3706300), Natural Science Foundation of Gansu Province (23JRRA1045) and the Fundamental Research Funds for the Central Universities (lzujbky-2024-jdzx07).

References

Allouche, M., Bou-Zeid, E., Ansorge, C., Katul, G. G., Chamecki, M., Acevedo, O., et al. (2022). The detection, genesis, and modeling of turbulence intermittency in the stable atmospheric surface layer. *Journal of the Atmospheric Sciences*, *79*(4), 1171–1190. https://doi.org/10.1175/JAS-D-21-0053.1

Banta, R. M. (2008). Stable-boundary-layer regimes from the perspective of the low-level jet. *Acta Geophysica*, *56*(1), 58–87. https://doi.org/10.2478/s11600-007-0049-8

Banta, R. M., Mahrt, L., Vickers, D., Sun, J., Balsley, B. B., Pichugina, Y. L., & Williams, E. J. (2007). The very stable boundary layer on nights with weak low-level jets. *Journal of the Atmospheric Sciences*, *64*(9), 3068–3090. https://doi.org/10.1175/jas4002.1

Banta, R. M., Pichugina, Y. L., & Brewer, W. A. (2006). Turbulent velocity-variance profiles in the stable boundary layer generated by a nocturnal low-level jet. *Journal of the Atmospheric Sciences*, *63*(11), 2700–2719. https://doi.org/10.1175/JAS3776.1

Barbano, F., Brogno, L., Tampieri, F., & Di Sabatino, S. (2022). Interaction between waves and turbulence within the nocturnal boundary layer. *Boundary-Layer Meteorology*, *183*(1), 35–65. https://doi.org/10.1007/s10546-021-00678-2

Barlow, J. F., Halios, C. H., Lane, S. E., & Wood, C. R. (2015). Observations of urban boundary layer structure during a strong urban heat island event. *Environmental Fluid Mechanics*, *15*(2), 373–398. https://doi.org/10.1007/s10652-014-9335-6

Bodini, N., Lundquist, J. K., Krishnamurthy, R., Pekour, M., Berg, L. K., & Choukulkar, A. (2019). Spatial and temporal variability of turbulence dissipation rate in complex terrain. *Atmospheric Chemistry and Physics*, *19*(7), 4367–4382. https://doi.org/10.5194/acp-19-4367-2019

Bonner, W. D. (1968). Climatology of the low level jet. *Monthly Weather Review*, *96*(12), 833–850. https://doi.org/10.1175/1520-0493(1968)096⟨0833:COTLLJ⟩2.0.CO;2

Borque, P., Luke, E., & Kollias, P. (2016). On the unified estimation of turbulence eddy dissipation rate using Doppler cloud radars and lidars. *Journal of Geophysical Research: Atmospheres*, *121*(10), 5972–5989. https://doi.org/10.1002/2015JD024543

Brunsell, N. A., Rahn, D. A., & Mechem, D. B. (2021). Impact of a nocturnal low-level jet on surface-layer turbulent characteristics. *Journal of Geophysical Research: Atmospheres*, *126*(7), e2020JD034083. https://doi.org/10.1029/2020JD034083

Businger, J. A. (1973). Turbulence transfer in the atmospheric surface layer. In *Workshop in Micro-meteorology* (pp. 67–100). American Meteorological Society.

Cava, D., Giostra, U., & Katul, G. G. (2015). Characteristics of gravity waves over an Antarctic ice sheet during an austral summer. *Atmosphere*, *6*(9), 1271–1289. https://doi.org/10.3390/atmos6091271

Cava, D., Mortarini, L., Anfossi, D., & Giostra, U. (2019). Interaction of submeso motions in the Antarctic stable boundary layer. *Boundary-Layer Meteorology*, *171*(2), 151–173. https://doi.org/10.1007/s10546-019-00426-7

Chan, P. W. (2010). LIDAR-based turbulence intensity calculation using glide-path scans of the Doppler Light Detection And Ranging (LIDAR) systems at the Hong Kong International Airport and comparison with flight data and a turbulence alerting system. *Meteorologische Zeitschrift*, *19*(6), 549–563. https://doi.org/10.1127/0941-2948/2010/0471

Chang, H., Ren, Y., Zhang, H., Liang, J., Cao, X., Tian, P., et al. (2024). The characteristics of turbulence intermittency and its impact on surface energy imbalance over Loess Plateau. *Agricultural and Forest Meteorology*, *354*, 110088. https://doi.org/10.1016/j.agrformet.2024.110088

Chemel, C., Staquet, C., & Largeron, Y. (2009). Generation of internal gravity waves by a katabatic wind in an idealized alpine valley. *Meteorology and Atmospheric Physics*, *103*(1–4), 187–194. https://doi.org/10.1007/s00703-009-0349-4

Corrêa, P. B., Dias-Júnior, C. Q., Cava, D., Sörgel, M., Botía, S., Acevedo, O. C., et al. (2021). A case study of a gravity wave induced by Amazon forest orography and low level jet generation. *Agricultural and Forest Meteorology*, *307*, 108457. https://doi.org/10.1016/j.agrformet.2021.108457

Ding, J., & Ren, Y. (2024). Data of low-level jet and internal gravity waves in the Zhongchuan International Airport in China [Dataset]. *Figshare*. https://doi.org/10.6084/m9.figshare.26413861.v1

Duarte, H. F., Leclerc, M. Y., Zhang, G., Durden, D. J., Kurzeja, R. J., Parker, M. J., & Werth, D. (2015). Impact of nocturnal low-level jets on near-surface turbulence kinetic energy. *Boundary-Layer Meteorology*, *156*(3), 349–370. https://doi.org/10.1007/s10546-015-0030-z

Fitzjarrald, D. R., & Moore, K. E. (1990). Mechanisms of nocturnal exchange between the rain forest and the atmosphere. *Journal of Geophysical Research*, *95*(D10), 16839–16850. https://doi.org/10.1029/JD095iD10p16839

Francone, C., Katul, G. G., Cassardo, C., & Richiardone, R. (2012). Turbulent transport efficiency and the ejection-sweep motion for momentum and heat on sloping terrain covered with vineyards. *Agricultural and Forest Meteorology*, *162–163*, 98–107. https://doi.org/10.1016/j.agrformet.2012.04.012

Frehlich, R., & Cornman, L. (2002). Estimating spatial velocity statistics with coherent Doppler lidar. *Journal of Atmospheric and Oceanic Technology*, *19*(3), 355–366. https://doi.org/10.1175/1520-0426-19.3.355

Frehlich, R., Meillier, Y., Jensen, M. L., Balsley, B., & Sharman, R. (2006). Measurements of boundary layer profiles in an urban environment. *Journal of Applied Meteorology & Climatology*, *45*(6), 821–837. https://doi.org/10.1175/JAM2368.1

Guo, X., Yang, W., Gao, Z., Wang, L., Hong, J., Ding, B., et al. (2022). Katabatic flow structures indicative of the flux dissimilarity for stable stratification. *Boundary-Layer Meteorology*, *182*(3), 379–415. https://doi.org/10.1007/s10546-021-00660-y

Hiscox, A., Bhimireddy, S., Wang, J. M., Kristovich, D. A. R., Sun, J. L., Patton, E. G., et al. (2023). Exploring influences of shallow topography in stable boundary layers: The SAVANT Field Campaign. *Bulletin of the American Meteorological Society*, *104*(2), E520–E541. https://doi.org/10.1175/BAMS-D-21-0332.1

Holton, J. R. (1967). The diurnal boundary layer wind oscillation above sloping terrain. *Tellus*, *19*(2), 200–205. https://doi.org/10.1111/j.2153-3490.1967.tb01473.x

Holtslag, A. A. M., Svensson, G., Baas, P., Basu, S., Beare, B., Beljaars, A. C. M., et al. (2013). Stable atmospheric boundary layers and diurnal cycles—Challenges for weather and climate models. *Bulletin of the American Meteorological Society*, *94*(11), 1691–1706. https://doi.org/10.1175/bams-d-11-00187.1

Kallistratova, M. A., & Kouznetsov, R. D. (2012). Low-level jets in the Moscow region in summer and winter observed with a Sodar network. *Boundary-Layer Meteorology*, *143*(1), 159–175. https://doi.org/10.1007/s10546-011-9639-8

Kim, J., Sharman, R., Strahan, M., Scheck, J. W., Bartholomew, C., Cheung, J. C. H., et al. (2018). Improvements in nonconvective aviation turbulence prediction for the World Area Forecast System. *Bulletin of the American Meteorological Society*, *99*(11), 2295–2311. https://doi.org/10.1175/BAMS-D-17-0117.1

Lemone, M. A., Angevine, W. M., Bretherton, C. S., Chen, F., Dudhia, J., Fedorovich, E., et al. (2018). 100 years of progress in boundary layer meteorology. *Meteorological Monographs*, *59*(9), 9.1–9.85. https://doi.org/10.1175/AMSMONOGRAPHS-D-18-0013.1

Luo, Z., & Fritts, D. C. (1993). Gravity-wave excitation by geostrophic adjustment of the jet stream. Part II: Three-dimensional forcing. *Journal of the Atmospheric Sciences*, *50*(1), 104–115. https://doi.org/10.1175/1520-0469(1993)050<0104:GWEBGA>2.0.CO;2

Mahrt, L. (1998). Nocturnal boundary-layer regimes. *Boundary-Layer Meteorology*, *88*(2), 255–278. https://doi.org/10.1023/A:1001171313493

Mahrt, L. (2010). Variability and maintenance of turbulence in the very stable boundary layer. *Boundary-Layer Meteorology*, *135*, 1–18. https://doi.org/10.1007/s10546-009-9463-6

Mahrt, L. (2014). Stably stratified atmospheric boundary layers. *Annual Review of Fluid Mechanics*, *46*(1), 23–45. https://doi.org/10.1146/annurev-fluid-010313-141354

Mahrt, L. (2019). Microfronts in the nocturnal boundary layer. *Quarterly Journal of the Royal Meteorological Society*, *145*(719), 546–562. https://doi.org/10.1002/qj.3451

Mahrt, L., & Bou-Zeid, E. (2020). Non-stationary boundary layers. *Boundary-Layer Meteorology*, *177*(2), 189–204. https://doi.org/10.1007/s10546-020-00533-w

Miao, Y., Guo, J., Liu, S., Wei, W., Zhang, G., Lin, Y., & Zhai, P. (2018). The climatology of low-level jet in Beijing and Guangzhou, China. *Journal of Geophysical Research: Atmospheres*, *123*(5), 2816–2830. https://doi.org/10.1002/2017JD027321

Mortarini, L., Cava, D., Giostra, U., Acevedo, O. C., Nogueira Martins, L. G., Soares de Oliveira, P. E., & Anfossi, D. (2018). Observations of submeso motions and intermittent turbulent mixing across a low-level jet with a 132-m tower. *Quarterly Journal of the Royal Meteorological Society*, *144*(710), 172–183. https://doi.org/10.1002/qj.3192

Mortarini, L., Cava, D., Giostra, U., Costa, F. D., Degrazia, G., Anfossi, D., & Acevedo, O. (2019). Horizontal meandering as a distinctive feature of the stable boundary layer. *Journal of the Atmospheric Sciences*, *76*(10), 3029–3046. https://doi.org/10.1175/JAS-D-18-0280.1

Muñoz-Esparza, D., Sharman, R. D., & Lundquist, J. K. (2018). Turbulence dissipation rate in the atmospheric boundary layer: Observations and WRF mesoscale modeling during the XPIA field campaign. *Monthly Weather Review*, *146*(1), 351–371. https://doi.org/10.1175/MWR-D-17-0186.1

Nappo, C. J. (2012). *An introduction to atmospheric gravity waves*, *International geophysics series* (2nd ed., Vol. 102, p. 276). Academic Press. https://doi.org/10.1016/b978-0-12-385223-6.00001-x

Ren, Y., Zhang, H., Zhang, L., & Liang, J. (2023). Quantitative description and characteristics of submeso motion and turbulence intermittency. *Quarterly Journal of the Royal Meteorological Society*, *149*(754), 1726–1744. https://doi.org/10.1002/qj.4479

Ren, Y., Zhang, H. S., Wei, W., Wu, B. G., Cai, X. H., & Song, Y. (2019). Effects of turbulence structure and urbanization on the heavy haze pollution process. *Atmospheric Chemistry and Physics*, *19*(2), 1041–1057. https://doi.org/10.5194/acp-19-1041-2019

Ren, Y., Zhang, H. S., Zhang, X. Y., Wei, W., Li, Q. H., Wu, B. G., et al. (2021). Turbulence barrier effect during heavy haze pollution events. *Science of the Total Environment*, *753*, 142286. https://doi.org/10.1016/j.scitotenv.2020.142286

Román-Cascón, C., Yagüe, C., Mahrt, L., Sastre-Marugán, M., Steeneveld, G.-J., Pardyjak, E. R., et al. (2015). Interactions among drainage flows, gravity waves and turbulence: A BLLAST case study. *Atmospheric Chemistry and Physics*, *15*(15), 9031–9047. https://doi.org/10.5194/acp-15-9031-2015

Roy, S., Sentchev, A., Schmitt, F. G., Augustin, P., & Fourmentin, M. (2021). Impact of the nocturnal low-level jet and orographic waves on turbulent motions and energy fluxes in the lower atmospheric boundary layer. *Boundary-Layer Meteorology*, *180*(3), 527–542. https://doi.org/10.1007/s10546-021-00629-x

Sarkar, S., & Scotti, A. (2017). From topographic internal gravity waves to turbulence. *Annual Review of Fluid Mechanics*, *49*(1), 195–220. https://doi.org/10.1146/annurev-fluid-010816-060013
Schiavon, M., Tampieri, F., Caggio, M., Mazzola, M., & Viola, A. P. (2023). The effect of submeso motions on the budgets of the mean turbulent kinetic energy and temperature variance in the stable atmospheric surface layer. *Boundary-Layer Meteorology*, *186*(3), 595–613. https://doi.org/10.1007/s10546-022-00774-x
Shapiro, A., Fedorovich, E., & Rahimi, S. (2016). A unified theory for the Great Plains nocturnal low-level jet. *Journal of the Atmospheric Sciences*, *73*(8), 3037–3057. https://doi.org/10.1175/JAS-D-15-0307.1
Shibuya, R., Sato, K., & Nakanishi, M. (2014). Diurnal wind cycles forcing inertial oscillations: A latitude-dependent resonance phenomenon. *Journal of the Atmospheric Sciences*, *71*(2), 767–781. https://doi.org/10.1175/JAS-D-13-0124.1
Smalikho, I. N., & Banakh, V. A. (2017). Measurements of wind turbulence parameters by a conically scanning coherent Doppler lidar in the atmospheric boundary layer. *Atmospheric Measurement Techniques*, *10*(11), 4191–4208. https://doi.org/10.5194/amt-10-4191-2017
Solanki, R., Guo, J., Lv, Y., Zhang, J., Wu, J., Tong, B., et al. (2022). Elucidating the atmospheric boundary layer turbulence by combining UHF radar wind profiler and radiosonde measurements over urban area of Beijing. *Urban Climate*, *43*, 101151. https://doi.org/10.1016/j.uclim.2022.101151
Stull, R. B. (1988). *An introduction to boundary layer meteorology*. *Atmospheric sciences library* (1st ed.). Springer.
Sun, J., Lenschow, D., Burns, S., Banta, R., Newsom, R., Coulter, R., et al. (2004). Atmospheric disturbances that generate intermittent turbulence in nocturnal boundary layers. *Boundary-Layer Meteorology*, *110*(2), 255–279. https://doi.org/10.1023/A:1026097926169
Sun, J., Mahrt, L., Banta, R. M., & Pichugina, Y. L. (2012). Turbulence regimes and turbulence intermittency in the stable boundary layer during cases-99. *Journal of the Atmospheric Sciences*, *69*(1), 338–351. https://doi.org/10.1175/jas-d-11-082.1
Sun, J., Nappo, C. J., Mahrt, L., Belušić, D., Grisogono, B., Stauffer, D. R., et al. (2015). Review of wave-turbulence interactions in the stable atmospheric boundary layer. *Reviews of Geophysics*, *53*(3), 956–993. https://doi.org/10.1002/2015RG000487
Sun, J. L., Lenschow, D. H., LeMone, M. A., & Mahrt, L. (2016). The role of large-coherent-eddy transport in the atmospheric surface layer based on CASES-99 observations. *Boundary-Layer Meteorology*, *160*(1), 83–111. https://doi.org/10.1175/jas-d-11-082.1
Sun, J. L., Mahrt, L., Nappo, C., & Lenschow, D. H. (2015). Wind and temperature oscillations generated by wave-turbulence interactions in the stably stratified boundary layer. *Journal of the Atmospheric Sciences*, *72*(4), 1484–1503. https://doi.org/10.1175/JAS-D-14-0129.1
Sutherland, B. R., Reeves, W., & van den Bremer, T. S. (2020). Flows induced by Coriolis-influenced vertically propagating two-dimensional internal gravity wave packets. *Physical Review Fluids*, *5*(6), 064805. https://doi.org/10.1103/PhysRevFluids.5.064805
Tsiringakis, A., Theeuwes, N. E., Barlow, J. F., & Steeneveld, G. J. (2022). Interactions between the nocturnal low-level jets and the urban boundary layer: A case study over London. *Boundary-Layer Meteorology*, *183*(2), 249–272. https://doi.org/10.1007/s10546-021-00681-7
Van der Linden, S. J., Wiel, B. J., Petenko, I., Heerwaarden, C. C., Baas, P., & Jonker, H. J. J. (2020). A Businger mechanism for intermittent bursting in the stable boundary layer. *Journal of the Atmospheric Sciences*, *77*(10), 3343–3360. https://doi.org/10.1175/JAS-D-19-0309.1
Viana, S., Terradellas, E., & Yagüe, C. (2010). Analysis of gravity waves generated at the top of a drainage flow. *Journal of the Atmospheric Sciences*, *67*(12), 3949–3966. https://doi.org/10.1175/2010JAS3508.1
Viana, S., Yagüe, C., Maqueda, G., & Morales, G. (2007). Study of the surface pressure fluctuations generated by waves and turbulence in the nocturnal boundary layer during SABLES2006 field campaign. *Física de la Tierra*, *19*, 55–71.
Viana, S., Yagüe, C., & Maqueda Burgos, G. (2012). Vertical structure of the stable boundary layer detected by RASS-SODAR and in-situ measurements in SABLES 2006 field campaign. *Acta Geophysica*, *60*(5), 1261–1286. https://doi.org/10.2478/s11600-011-0072-7
Wallace, J. M. (2016). Quadrant analysis in turbulence research: History and evolution. *Annual Review of Fluid Mechanics*, *48*(1), 131–158. https://doi.org/10.1146/annurev-fluid-122414-034550
Wallace, J. M., Eckelmann, H., & Brodkey, R. S. (1972). The wall region in turbulent shear flow. *Journal of Fluid Mechanics*, *54*(1), 39–48. https://doi.org/10.1017/S0022112072000515
Wei, W., Zhang, H., Zhang, X., & Che, H. (2023). Low-level jets and their implications on air pollution: A review. *Frontiers in Environmental Science*, *10*, 1082623. https://doi.org/10.3389/fenvs.2022.1082623
Wei, Z., Zhang, H., Wei, W., Zhang, X., Cai, X., Song, Y., & Zhu, T. (2022). Mechanism of the effect of vertically propagating internal gravity waves on turbulence barrier and pollutant diffusion during heavy haze episodes. *Science of The Total Environment*, *845*, 157349. https://doi.org/10.1016/j.scitotenv.2022.157349
Wei, Z., Zhang, L., Ren, Y., Wei, W., Zhang, H., Cai, X., et al. (2021). Characteristics of the turbulence intermittency and its influence on the turbulent transport in the semi-arid region of the loess plateau. *Atmospheric Research*, *249*, 105312. https://doi.org/10.1016/j.atmosres.2020.105312
Whiteman, C. D., Bian, X., & Zhong, S. (1997). Low-level jet climatology from enhanced rawinsonde observations at a site in the southern Great Plains. *Journal of Applied Meteorology*, *36*(10), 1363–1376. https://doi.org/10.1175/1520-0450(1997)036<1363:LLJCFE>2.0.CO;2
Wilczak, J. M., Stoelinga, M., Berg, L. K., Sharp, J., Draxl, C., McCaffrey, K., et al. (2019). Estimation of turbulence dissipation rate from Doppler wind lidars and in situ instrumentation for the Perdigão 2017 campaign. *Atmospheric Measurement Techniques*, *12*(12), 6401–6423. https://doi.org/10.5194/amt-12-6401-2019
Wildmann, N., Bodini, N., Lundquist, J. K., Bariteau, L., & Wagner, J. (2019). Estimation of turbulence dissipation rate from Doppler wind lidars and in situ instrumentation for the Perdigo 2017 campaign. *Atmospheric Measurement Techniques*, *2019*(12), 6401–6423. https://doi.org/10.5194/amt-12-6401-2019
Zilitinkevich, S. S., Elperin, T., Kleeorin, N., & Rogachevskii, I. (2007). Energy- and flux-budget (EFB) turbulence closure model for stably stratified flows. Part I: Steady-state, homogeneous regimes. *Boundary-Layer Meteorology*, *125*, 167–191. https://doi.org/10.1007/978-0-387-74321-9_3